



Irradiation origin of ^{10}Be in the solar nebula: Evidence from Li-Be-B and Al-Mg isotope systematics, and REE abundances of CAIs from Yamato-81020 CO3.05 chondrite

Kohei Fukuda^{a,b,*}, Hajime Hiyagon^a, Wataru Fujiya^c, Takanori Kagoshima^{d,g},
Keita Itano^{a,f}, Tsuyoshi Iizuka^a, Noriko T. Kita^b, Yuji Sano^{d,e}

^a Department of Earth and Planetary Science, The University of Tokyo, 7-3-1 Hongo, Bunkyo, Tokyo 113-0033, Japan

^b WiscSIMS, Department of Geoscience, University of Wisconsin-Madison, 1215 W. Dayton St., Madison, WI 53706, USA

^c Faculty of Science, Ibaraki University, 2-1-1 Bunkyo, Mito, Ibaraki 310-8512, Japan

^d Atmosphere and Ocean Research Institute, The University of Tokyo, 5-1-5 Kashiwanoha, Kashiwa, Chiba 277-8564, Japan

^e Institute of Surface-Earth System Science, Tianjin University, Tianjin 300072, People's Republic of China

^f College of Science and Engineering, Kanazawa University, Kanazawa 920-1192, Japan¹

^g Department of Environmental Biology and Chemistry, School of Science, University of Toyama, Toyama 930-8555, Japan¹

Received 9 June 2020; accepted in revised form 9 October 2020; available online 20 October 2020

Abstract

We have performed *in situ* analyses of Li-Be-B and Al-Mg isotope systematics, and abundances of rare earth elements (REEs) in two Ca-Al-rich inclusions (CAIs) from the Ornans-like carbonaceous chondrite Yamato-81020 (CO3.05). The present CO CAIs are depleted in ultra-refractory heavy REEs (group II REE pattern), suggesting condensation of these CAIs or their precursors from the solar nebula. Initial $^{26}\text{Al}/^{27}\text{Al}$ ratios, $(^{26}\text{Al}/^{27}\text{Al})_0$, of these CO CAIs are found to be $(4.8 \pm 0.5) \times 10^{-5}$ and $(4.9 \pm 0.3) \times 10^{-5}$ (95% confidence), indicating their contemporaneous formation with a majority of CAIs from Vigarano-like carbonaceous (CV) chondrites. Melilite grains in the present CO CAIs show clear excesses in ^{10}B , ranging from ~ 370 to $\sim 4300\%$ relative to the chondritic B isotopic composition, which are correlated well with $^9\text{Be}/^{11}\text{B}$ ratios. The correlation indicates *in situ* decay of ^{10}Be in the present CO CAIs and yields initial $^{10}\text{Be}/^9\text{Be}$ ratios, $(^{10}\text{Be}/^9\text{Be})_0$, for the individual CAIs of $(2.9 \pm 0.6) \times 10^{-3}$ and $(2.2 \pm 1.0) \times 10^{-3}$ (95% confidence), which are significantly greater than the average $(^{10}\text{Be}/^9\text{Be})_0 = \sim 0.7 \times 10^{-3}$ recorded in CAIs from CV chondrites. The apparent variation in $(^{10}\text{Be}/^9\text{Be})_0$ between the CO and CV CAIs, despite having indistinguishable $(^{26}\text{Al}/^{27}\text{Al})_0$ of $\sim 5 \times 10^{-5}$, provides evidence for heterogeneous distribution of ^{10}Be in the CAI forming-regions at the very beginning of the Solar System. The elevated $(^{10}\text{Be}/^9\text{Be})_0$ and group II REE patterns in the CO CAIs may reflect that compared with the CV CAIs having unfractionated REEs the present CO CAIs have formed closer to the Sun where ^{10}Be was produced more efficiently through solar cosmic ray irradiation caused by solar flares. Alternatively, if the present CO CAIs and CV CAIs formed in the same region, and ^{26}Al was distributed homogeneously at the CAI-forming region, our results indicate that solar cosmic ray fluxes at the forming region have fluctuated by a factor of six within a short duration (~ 0.2 million years) inferred from the Al-Mg chronology.

© 2020 Elsevier Ltd. All rights reserved.

Keywords: Ca-Al-rich inclusions; Rare earth elements; Short-lived radionuclides; Cosmic ray interaction; Early Solar System

* Corresponding author at: WiscSIMS, Department of Geoscience, University of Wisconsin-Madison, 1215 W. Dayton St., Madison, WI 53706, USA.

E-mail address: kfukuda2@wisc.edu (K. Fukuda).

¹ Present address.

1. INTRODUCTION

Understanding the origin and distribution of short-lived radionuclides (SLRs) in the early Solar System provides important constraints on the astrophysical environment of the earliest stage of the Solar System evolution (Davis and McKeegan, 2014; Chaussidon and Liu, 2015). The presence of a SLR beryllium-10 ($T_{1/2} = 1.39$ million years, Myr; Korschinek et al., 2010) has been inferred from ^{10}Be - ^{10}B isotope analyses of Ca-Al-rich inclusions (CAIs) (McKeegan et al., 2000) which are thought to be the oldest solids formed in the Solar System (Amelin et al., 2010; Bouvier and Wadhwa, 2010; Connelly et al., 2012). Unlike other SLRs (e.g., ^{26}Al and ^{60}Fe), ^{10}Be cannot be synthesized by thermonuclear reactions in stars (Fowler et al., 1961). Instead, non-thermal nuclear reactions between energetic particles and target materials (i.e., gas and/or dust) could produce ^{10}Be (e.g., Gounelle et al., 2001, 2006; Leya et al., 2003; Bricker and Caffee, 2010; Jacquet, 2019). Thus, the presence of ^{10}Be may be a key to understand cosmic ray interactions at the earliest stage of the Solar System evolution.

To date, however, the origin of ^{10}Be in the early Solar System is still controversial. Ion microprobe studies on Li-Be-B isotope systematics of coarse-grained CAIs from Vigarano-like (CV) chondrites and refractory hibonite ($\text{CaAl}_{12}\text{O}_{19}$) grains from the Murchison (Mighei-like; CM) chondrite revealed variations in initial $^{10}\text{Be}/^9\text{Be}$ ratios ($\sim 3\text{--}10 \times 10^{-4}$; McKeegan et al., 2000; Sugiura et al., 2001; Marhas et al., 2002; MacPherson et al., 2003; Chaussidon et al., 2006; Liu et al., 2009, 2010; Wielandt et al., 2012; Srinivasan and Chaussidon, 2013). Among them, initial $^{10}\text{Be}/^9\text{Be}$ ratios of CV CAIs with near canonical $^{26}\text{Al}/^{27}\text{Al}$ ratios ($\sim 4\text{--}5 \times 10^{-5}$) range from $(4.8 \pm 1.7) \times 10^{-4}$ to $(8.8 \pm 0.6) \times 10^{-4}$ (2σ), which vary by a factor of 2 (MacPherson et al., 2003; Chaussidon et al., 2006; Srinivasan and Chaussidon, 2013). The variation in initial $^{10}\text{Be}/^9\text{Be}$ ratios of the near canonical CAIs suggests a heterogeneous distribution of ^{10}Be at the CV CAI-forming region, which is consistent with a solar cosmic ray irradiation origin of ^{10}Be (e.g., McKeegan et al., 2000; Gounelle et al., 2001, 2006; Goswami et al., 2001; Marhas et al., 2002; Leya et al., 2003; Bricker and Caffee, 2010; Jacquet, 2019). Srinivasan and Chaussidon (2013) provided detailed discussion on the origin of the variation in initial $^{10}\text{Be}/^9\text{Be}$ ratios based on the relationship between initial $^{10}\text{Be}/^9\text{Be}$ ratios and supra-chondritic initial $^{10}\text{B}/^{11}\text{B}$ ratios among CV CAIs. Since the energetic particle interaction could produce ^{10}Be as well as stable isotopes of Li, Be, and B (Reeves, 1994 and references therein; see also a recent review by Liu and Chaussidon, 2018 for B isotopes), Srinivasan and Chaussidon (2013) attributed the variable $^{10}\text{Be}/^9\text{Be}$ ratios and supra-chondritic initial B isotope ratios in the CV CAIs to heterogeneous production/distribution of ^{10}Be in the solar protoplanetary disk. Additionally, studies on CAIs from metal-rich carbonaceous chondrites (CH and CH/CB) have shown larger variations in initial $^{10}\text{Be}/^9\text{Be}$ ratios ($\sim 0\text{--}100 \times 10^{-4}$; Gounelle et al., 2013; Fukuda et al., 2019), further indicative of the solar cosmic ray irradiation origin of ^{10}Be . In addition to ^{10}Be , the presence of

the SLR ^7Be has been inferred from Li-Be-B isotope systematics of CV CAIs (Chaussidon et al., 2006; Mishra and Marhas, 2019). Because ^7Be has a half-life of 53 days (Jaeger et al., 1996), the result requires very short time intervals between the production of ^7Be and its incorporation into a CAI-forming reservoir. Thus, the co-presence of ^7Be and ^{10}Be in CAIs could be a stringent constraint on their production by the solar cosmic ray irradiation. Recently, in contrast, Dunham et al. (2019) proposed a homogeneous distribution of ^{10}Be ($^{10}\text{Be}/^9\text{Be} = \sim 7 \times 10^{-4}$) in the solar nebula, based on the statistical data reduction of previous studies (Dunham et al., 2020) and their new Be-B dataset of CAIs from Ornans-like (CO) and CH/CB chondrites. The homogeneous distribution of ^{10}Be favors a hypothesis that ^{10}Be was inherited from the parental molecular cloud of the Solar System that has been irradiated by galactic cosmic rays (Desch et al., 2004). Alternatively, Banerjee et al. (2016) demonstrated that ^{10}Be can be synthesized in low-mass supernovae by neutrino spallation reactions. These new observations and theoretical studies call for a reconsideration of the origin of ^{10}Be in the early Solar System.

Most of the initial ^{10}Be abundance data available so far were deduced from the ^{10}Be - ^{10}B analyses of CAIs from CV chondrites because their large sizes (commonly centimeter-sized or even larger; MacPherson, 2014) allow multi-spot ion microprobe analyses within individual inclusions (McKeegan et al., 2000; Sugiura et al., 2001; MacPherson et al., 2003; Chaussidon et al., 2006; Wielandt et al., 2012; Srinivasan and Chaussidon, 2013; Sossi et al., 2017; Mishra and Marhas, 2019). Note, however, that these large CAIs are rare in other chondrites and, therefore, would not be representative of the entire CAI population. To better understand the origin and distribution of ^{10}Be in the early Solar System, Be-B systematics of CAIs from various types of chondrites should be investigated.

Here we report Li-Be-B and Al-Mg isotope systematics of two melilite-rich CAIs from the CO chondrite Yamato-81020 (hereafter Y-81020) that is one of the least metamorphosed carbonaceous chondrites (petrologic type 3.05; Grossman and Brearley, 2005; Grossman and Rubin, 2006; Kimura et al., 2008). CAIs from Y-81020 show no textural evidence of secondary alteration on the parent body (Mishra, 2018) so that these CAIs are expected to preserve pristine Li-Be-B and Al-Mg isotopic signatures. Melilite-rich CAIs are most common among CO chondrites, which are similar to Type A CAIs from CV chondrites (Grossman, 1975; MacPherson and Grossman, 1984; Simon et al., 1999), although smaller in size (typically $< 500 \mu\text{m}$) (e.g., Russell et al., 1998; Simon and Grossman, 2015; Zhang et al., 2020). A recent Al-Mg isotope study of small CAIs ($< 100 \mu\text{m}$ in size) from CO3.03 chondrite Allan Hills A77307 identified two main populations in terms of initial $^{26}\text{Al}/^{27}\text{Al}$ ratios [$(5.4 \pm 0.1) \times 10^{-5}$ and $(4.9 \pm 0.1) \times 10^{-5}$; Liu et al., 2019]. The two main populations are marginally resolved from the well-constrained canonical $^{26}\text{Al}/^{27}\text{Al}$ ratio of $(5.2 \pm 0.1) \times 10^{-5}$ characterizing CAIs from CV chondrites (Bizzarro et al., 2004; Jacobsen et al., 2008; Larsen et al., 2011, 2020). Therefore, CAIs from CO and CV chondrites may record different

early Solar System histories. Recently, [Sossi et al. \(2017\)](#) conducted a correlated study of Be-B and vanadium isotope analyses, and rare earth element (REE) abundances of CAIs from CV chondrites (Allende and NWA 8616). They found that fine-grained CAIs with a group II CI-normalized REE pattern, which is characterized by depletion in ultra-refractory heavy REEs ([Martin and Mason, 1974](#); [Boynnton, 1975](#); [Davis and Grossman, 1979](#)), tend to have higher initial $^{10}\text{Be}/^9\text{Be}$ ratios ($^{10}\text{Be}/^9\text{Be} = \sim 70 \times 10^{-4}$) than those of coarse-grained CAIs with an unfractionated REE pattern ($^{10}\text{Be}/^9\text{Be} = \sim 12 \times 10^{-4}$). These observations imply different irradiation conditions for each CAI population. In the present study, we also included REE analyses for the two CO CAIs to see possible relationships between REE abundances and Li-Be-B isotope systematics. Based on a newly obtained dataset in this study, together with the data of previous studies, the origin and distribution of ^{10}Be at the CAI-forming region(s) are discussed.

2. MATERIAL AND METHODS

2.1. Sample and electron microscopic analyses

Two thin sections of Y-81020 were searched with a JEOL JXA-8530F field emission electron probe microanalyzer (FE-EPMA) at the Department of Earth and Planetary Science, University of Tokyo. Two melilite-rich CAIs, Y20-1X1 ([Fig. 1](#)) and Y20-9-1 ([Fig. 2](#)), were selected for REE and isotopic measurements. X-ray elemental maps of the two CAIs were obtained with the FE-EPMA, which were performed with a fully focused electron beam, 15 kV accelerating voltage, 80 nA beam current, 30 μs per pixel acquisition time, and spatial resolution of ~ 0.7 – $1.5 \mu\text{m}$ per pixel. Major element concentrations (Na_2O , MgO , Al_2O_3 , SiO_2 , K_2O , CaO , TiO_2 , V_2O_5 , Cr_2O_3 , MnO , FeO , and NiO) of minerals in the two CAIs were obtained with the FE-EPMA, which were performed with a 1 μm focused electron beam, 15 kV accelerating voltage, and 12 nA beam current. Calculated detection limits (99% confidence) for the measured oxides were Na_2O -0.11, MgO -0.11, Al_2O_3 -

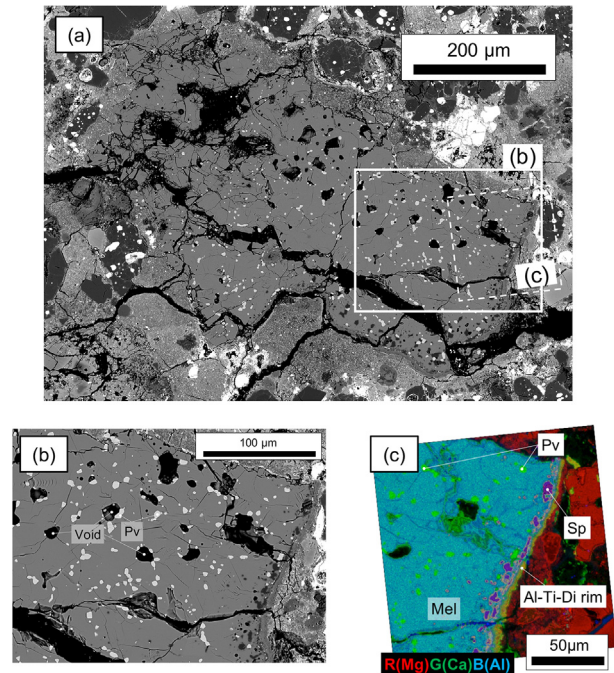


Fig. 2. BSE images and a combined X-ray map of melilite-rich CAI Y20-9-1 from Yamato-81020 (CO3.05) chondrite. For a figure (c), Mg is shown in red, Ca is shown in green, and Al is shown in blue. Solid and dashed rectangles in a figure (a) indicate areas shown as expanded views in (b) and (c), respectively. Sp = spinel; Mel = melilite; Al-Ti-Di = Aluminum, Titanium-rich diopside; Pv = perovskite.

0.11, SiO_2 -0.14, K_2O -0.07, CaO -0.10, TiO_2 -0.19, V_2O_5 -0.12, Cr_2O_3 -0.14, MnO -0.18, FeO -0.17, and NiO -0.17 wt%.

2.2. REE measurements

REE abundances of the two CAIs were investigated using an iCAP Qc inductively coupled plasma mass spectrometer (ICP-MS) with a Nd:YAG laser ablation (LA) system at the Department of Earth and Planetary Science,

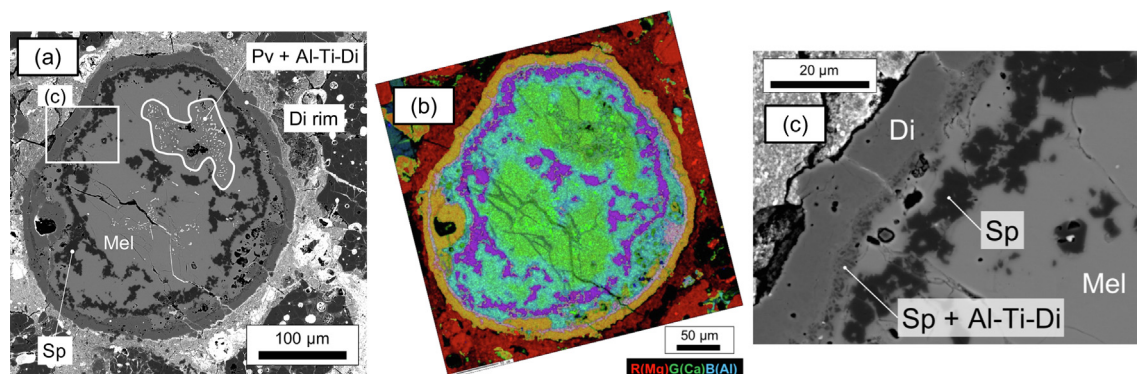


Fig. 1. BSE images and a combined X-ray map of melilite-rich CAI Y20-1X1 from Yamato-81020 (CO3.05) chondrite. For a figure (b), Mg is shown in red, Ca is shown in green, and Al is shown in blue. A white rectangle in a figure (a) indicates an area shown as an expanded view in (c). Sp = spinel; Mel = melilite; (Al-Ti-) Di = (Aluminum, Titanium-rich) diopside; Pv = perovskite.

University of Tokyo. The measured ion species and operating conditions of the LA system and ICP-MS are listed in Table A1 ([Electronic Annex EA1](#)). The LA-ICP-MS measurements were performed in spot analysis mode (~25–30 μm in diameter). The instrumental parameters were set so that the oxide production rate of Th (ThO^+/Th^+) was smaller than 1% ([Itano and Iizuka, 2017](#)). Each of two unknown analyses was bracketed by three measurements of a NIST SRM 612 glass standard that was used for the correction of relative sensitivities of measured ion species. An aliquot of BCR-2G glass was measured as a secondary standard. Ion signals of $^{43}\text{Ca}^+$ were used for internal normalization. External reproducibilities of REE^+/Ca^+ for NIST SRM 612 were smaller than $\pm 10\%$ (2 standard deviation; 2SD) during a session. Internal errors (2 standard error; 2SE) are assigned as uncertainties on unknown analyses, which were larger than the external reproducibilities ($\pm 10\%$, 2SD) because of their lower count rates.

2.3. Al-Mg isotope measurements

The Al-Mg isotope analyses of melilite, spinel, and diopside were performed with the WiscSIMS Cameca IMS 1280 secondary ion mass spectrometer (SIMS) at the University of Wisconsin-Madison equipped with a radio-frequency (RF) plasma ion source. The analytical conditions are similar to those described in [Kita et al. \(2012\)](#) and [Fukuda et al. \(2020\)](#) except for the primary beam conditions and the use of lower-noise feedback resistors for Faraday cups (FCs) ([Fukuda et al., 2021](#)). We prepared two $^{16}\text{O}_2^-$ primary ion beam settings for analyses of melilite ($8 \times 10 \mu\text{m}$, 2 nA), and spinel and diopside ($4 \times 5 \mu\text{m}$, 0.3 nA). Secondary ions ($^{24}\text{Mg}^+$, $^{25}\text{Mg}^+$, $^{26}\text{Mg}^+$, and $^{27}\text{Al}^+$) were detected simultaneously on multi-collector FCs (L/2, C, H1, and H/2) using three 10^{12} ohm and one 10^{11} ohm resistors for $^{24,25,26}\text{Mg}^+$ and $^{27}\text{Al}^+$, respectively. The mass resolving power (MRP) at 10% peak height was set to ~ 2500 (entrance slit; 90 μm and exit slit 500 μm) and interferences of $^{48}\text{Ca}^{2+}$ and $^{24}\text{Mg}^1\text{H}^+$ onto $^{24}\text{Mg}^+$ and $^{25}\text{Mg}^+$ peaks were negligibly small. The energy slit was set to 50 eV width. Matrix matched standards of melilite glasses ($\text{\AA}k_{15}$ and $\text{\AA}k_{35}$), diopside (95AK-6 Di), and spinel were used as bracketing standards. These standards, as well as additional melilite glasses ($\text{\AA}k_{25}$ and $\text{\AA}k_{65}$) and pyroxene (IG-Cpx) standards, were analyzed to correct instrumental mass fractionations (IMFs) of Mg isotopes, and determine relative sensitivity factors (RSFs) of $^{27}\text{Al}/^{24}\text{Mg}$ ratios. $\delta^{25}\text{Mg}_{\text{DSM-3}}$ values of these standards, except for spinel (where $\delta^{25}\text{Mg}_{\text{DSM-3}} = [({}^{25}\text{Mg}/{}^{24}\text{Mg})_{\text{sample}}/({}^{25}\text{Mg}/{}^{24}\text{Mg})_{\text{DSM-3}} - 1] \times 1000$; per-mil deviation from Mg reference material DSM-3; [Galy et al., 2003](#)), have been determined by solution nebulization multi-collector ICP-MS (MC-ICP-MS), which were reported in [Kita et al. \(2012\)](#) and [Fukuda et al. \(2020\)](#). Mg isotope analysis of the spinel standard by MC-ICP-MS is in progress but not available at present, so that the $\delta^{25}\text{Mg}_{\text{DSM-3}}$ value of the spinel standard is assumed to be 0 in this study. For melilite analyses, a single analysis took ~ 8 min, including 100 s of presputtering, ~ 80 s for automated centering of the secondary ion deflectors (DTFA-X and -Y), and 300 s of integration ($10 \text{ s} \times 30$ cycles) of the

secondary ion signals. For spinel and diopside analyses, 500 s of integration ($10 \text{ s} \times 50$ cycles) was employed so that a single analysis took ~ 12 min. The typical $^{24}\text{Mg}^+$ and $^{27}\text{Al}^+$ count rates during measurement of the melilite glass standard ($\text{\AA}k_{35}$) were 2.1×10^7 and 8.8×10^7 cps, respectively. Those of the spinel standard were 2.3×10^7 and 4.6×10^7 cps, respectively, and those of the diopside (95AK-6 Di) standard were 1.7×10^7 and 8.5×10^5 cps, respectively. The baselines of four FCs were monitored during each presputtering and averaged over eight analyses. The standard deviations of FC baselines over eight analyses were typically 140 cps for L/2, C, and H1, and 530 cps for H/2, corresponding to 7×10^{-6} relative to $^{24}\text{Mg}^+$, 5×10^{-5} relative to $^{25}\text{Mg}^+$ and $^{26}\text{Mg}^+$, and 6×10^{-6} relative to $^{27}\text{Al}^+$ ion intensities of the melilite glass standard ($\text{\AA}k_{35}$). Data reduction procedures follow those described in [Ushikubo et al. \(2017\)](#) and are summarized in [Electronic Annex EA2](#). The typical external reproducibilities (2SD) of $\delta^{25}\text{Mg}$, $\delta^{26}\text{Mg}$, and $\Delta^{26}\text{Mg}$ for the melilite glass standards ($\text{\AA}k_{15}$ and $\text{\AA}k_{35}$) were $\leq 0.20\text{‰}$, $\leq 0.25\text{‰}$, and $\leq 0.35\text{‰}$, respectively. Those for the diopside and spinel standards were $\leq 0.18\text{‰}$, $\leq 0.27\text{‰}$ and $\leq 0.25\text{‰}$, respectively.

2.4. Li-Be-B isotope measurements

The Be-B isotope analyses of melilite and diopside were performed with a Cameca NanoSIMS 50 at Atmosphere and Ocean Research Institute (AORI), University of Tokyo. The analytical conditions are the same as those described in [Fukuda et al. \(2019\)](#), except for primary ion beam conditions. We prepared three $^{16}\text{O}^-$ primary ion beam settings for analyses of melilite ($8 \times 8 \mu\text{m}$, 3 nA and $10 \times 10 \mu\text{m}$, 5 nA) and diopside ($5 \times 5 \mu\text{m}$, 1 nA). To remove carbon coating and surface boron contamination, we presputtered the samples for 10 min before the measurements. For the presputtering, the $^{16}\text{O}^-$ primary ion beam of 5 nA was rastered over $15 \times 15 \mu\text{m}^2$ areas on the samples for 5 min, and then central parts ($10 \times 10 \mu\text{m}^2$) within the areas were presputtered for additional 5 min. Afterward, the primary ion beam was rastered over the presputtered $10 \times 10 \mu\text{m}^2$ areas for the measurements. Secondary ions of $^9\text{Be}^+$, $^{10}\text{B}^+$, $^{11}\text{B}^+$, and $^{30}\text{Si}^+$ were detected simultaneously with four electron multipliers (EMs). For melilite analyses with the primary ion beam of 5 nA, the typical count rates were ~ 40 cps for $^9\text{Be}^+$, ~ 0.2 cps for $^{10}\text{B}^+$, and 1.0×10^5 cps for $^{30}\text{Si}^+$. The MRP at 1% peak height was set to ~ 1500 , sufficient to separate $^9\text{Be}^1\text{H}^+$ from $^{10}\text{B}^+$ and $^{10}\text{B}^1\text{H}^+$ from $^{11}\text{B}^+$. Secondary ion signals from the center of the sputtered areas (24×24 pixels out of 32×32 pixels; i.e., a $\sim 56\%$ electronic beam blanking was applied) were collected to avoid contributions from scattered ions from the surrounding area ([Fujiya et al., 2016](#)). The measurement time was up to ~ 70 min for the samples, dependent on the ^{10}B count rate. After each measurement, the backgrounds of four EMs were monitored on each analytical spot for 17 min, which were typically ~ 0.03 cps. The RSFs of Be/B, Be/Si, and B/Si were determined by multiple measurements of a NIST SRM 610 glass standard, for which $^9\text{Be}/^{11}\text{B}$ RSF is identical to that for synthetic melilite glasses within

uncertainties (Fukuda et al., 2018; Dunham et al., 2020). The IMF on $^{10}\text{B}/^{11}\text{B}$ was corrected using the NIST SRM 610 ($^{10}\text{B}/^{11}\text{B} = 0.2474$; Brand et al., 2014).

After the Be-B analyses, Li isotope analyses of melilite were performed under the same secondary ion optics for the Be-B analyses, but moving EMs to certain positions. Two $^{16}\text{O}^-$ primary ion beams ($8 \times 8 \mu\text{m}$, 3 nA and $10 \times 10 \mu\text{m}$, 5 nA) were used for the analyses. Prior to the measurements, the samples were presputtered with a primary ion beam of 3 or 5 nA that was rastered over $10 \times 10 \mu\text{m}^2$ areas for ~ 5 –10 min. Secondary ions of $^6\text{Li}^+$, $^7\text{Li}^+$, and $^{30}\text{Si}^+$ were detected simultaneously with three EMs. The count rates of $^6\text{Li}^+$ and $^{30}\text{Si}^+$ range from ~ 2 to 50 cps and 0.4×10^5 to 1.4×10^5 cps, respectively. As for Be-B analyses, electronic beam blanking was applied so that secondary ions from the center of the sputtered areas were collected. The measurement time was up to ~ 50 min for the samples, dependent on the Li count rates. The observed $^7\text{Li}/^6\text{Li}$ ratios and Li elemental abundances of melilite were normalized to those of a NIST SRM 612 glass standard, which has a $^7\text{Li}/^6\text{Li}$ ratio = 12.553 (Kasemann et al., 2005) and Li concentration of 40.2 ppm (Jochum et al., 2011). The present Li-Be-B data ($^7\text{Li}/^6\text{Li}$, $^9\text{Be}/^{11}\text{B}$, and $^{10}\text{B}/^{11}\text{B}$ ratios and elemental concentrations) were obtained by summing up secondary ion signals over the entire analysis (Ogliore et al., 2011). Uncertainties of these data were determined based on counting statistics for the total count numbers of the secondary ion signals.

3. RESULTS

3.1. Mineralogy and REE abundances

Representative major element compositions are listed in Table A2 (Electronic Annex EA1). REE concentrations are listed in Table A3 (Electronic Annex EA1). Locations of REE, Al-Mg, and Li-Be-B analyses within CAIs are shown in Electronic Annex EA3.

CAI Y20-1X1, $\sim 300 \times 300 \mu\text{m}$ in size, is a melilite-rich CAI that has a rounded shape (Fig. 1a). This CAI is composed mostly of melilite (>80 vol%, estimated by using composite elemental maps and *ImageJ* software; Ferreira and Rasband, 2012) and anhedral spinel (~ 16 vol%) and minor perovskite grains. Perovskite grains are often enclosed by Al-Ti-rich diopside (Fig. 1a). Melilite shows chemical zoning with åkermanite contents increasing from an outer spinel layer ($\sim \text{Åk}_{34}$) to the CAI interior ($\sim \text{Åk}_{55}$) (Fig. 1b). No secondary minerals such as nepheline are found. The CAI is surrounded by a double-layered rim of thinner spinel + Al-Ti-rich diopside layer ($\sim 5 \mu\text{m}$) and thicker magnesian diopside layer ($\sim 15 \mu\text{m}$, Fig. 1c). Similar objects have been found in the same meteorite (CAI 18; Mishra, 2018) and another CO chondrite DOM 08004 (Inclusion 26–2; Simon and Grossman, 2015). The Y20-1X1 has a modified group II REE pattern in melilite as well as a perovskite-rich portion (Fig. 3; normalized to REE abundances in CI), which is characterized by depletion in ultra-refractory heavy REEs (HREEs) with positive anomalies in Ce, (Eu), and Yb (Hiyagon et al., 2011). REE concentrations of melilite are ~ 1 –2 orders of magni-

tude lower than those of perovskite + Al-Ti-rich diopside (+minor melilite) portions except for Eu (Fig. 3).

CAI Y20-9-1, $\sim 650 \times 400 \mu\text{m}$ in size, is an irregular-shaped melilite-rich CAI (Fig. 2a), which appears to be a fragment of a larger CAI. Melilite grains have gehlenitic compositions (Åk_{4-11}). Minor perovskite grains are also observed, some of which occur around the voids (Fig. 2b). Anhedral spinel grains are concentrated close to the edge of the CAI (Fig. 2c). Melilite close to the rim has more gehlenitic compositions (Åk_{4-5}) than that of the CAI interior (Åk_{7-11}). No secondary minerals such as nepheline are found. This CAI is surrounded by a double-layered rim of discontinuous spinel + Al-Ti-rich diopside layer and Al-Ti-rich diopside layer (Fig. 2c). Melilite in Y20-9-1 has a modified group II REE pattern (Fig. 3). The mineralogy and texture of this CAI are similar to CAI G104 from Acfer 094 (ungrouped C3.00) that was described by Ushikubo et al. (2017).

3.2. Al-Mg isotope systematics

Magnesium isotope ratios ($\delta^{25}\text{Mg}_{\text{DSM-3}}$ and $\delta^{26}\text{Mg}^*$) and $^{27}\text{Al}/^{24}\text{Mg}$ ratios are given in Table 1. All individual data, including analyses of standards, are listed in Electronic Annex EA4. The $\delta^{26}\text{Mg}^*$ values of melilite in the present CO CAIs are linearly correlated with $^{27}\text{Al}/^{24}\text{Mg}$ ratios (Fig. 4). Data for melilite and spinel in Y20-1X1 form a well-defined linear regression line (Fig. 4a). Initial $^{26}\text{Al}/^{27}\text{Al}$ ratios and initial $\delta^{26}\text{Mg}^*$ values were deduced from isochron regressions (Isoplot 4.15 model 1 fit, Ludwig, 2012). Uncertainties in initial $^{26}\text{Al}/^{27}\text{Al}$ ratios and initial

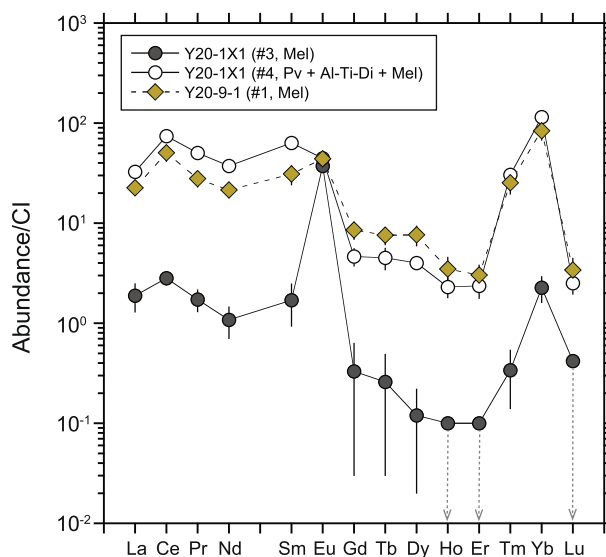


Fig. 3. Representative CI-normalized (McDonough and Sun, 1995) REE abundances in two CAIs (Y20-1X1 and Y20-9-1) from Yamato-81020 (CO3.05) chondrite. For clarity, selected data are shown in this figure. All data are plotted in Fig. A1 (Electronic Annex EA2). Note that only upper limits (2 standard error: 2SE) for Ho, Er, and Lu are shown for the melilite analysis of Y20-1X1 (#3) by arrows. Error bars are 2SE. Mel = melilite; Al-Ti-Di = Aluminum, Titanium-rich diopside; Pv = perovskite.

$\delta^{26}\text{Mg}^*$ values are 95% confidence limits. The inferred initial $^{26}\text{Al}/^{27}\text{Al}$ ratios, $(^{26}\text{Al}/^{27}\text{Al})_0$, of Y20-1X1 and Y20-9-1 are $(4.8 \pm 0.5) \times 10^{-5}$ (MSWD = 0.3) and $(4.9 \pm 0.3) \times 10^{-5}$ (MSWD = 1.3), respectively. These $(^{26}\text{Al}/^{27}\text{Al})_0$ values are not resolvable from the canonical value $[(5.2 \pm 0.1) \times 10^{-5}$; Jacobsen et al., 2008; Larsen et al., 2011] and one of the main population observed in CAIs from another CO chondrite Allan Hills A77307 $[(4.9 \pm 0.1) \times 10^{-5}$; Liu et al., 2019]. Intercepts of the regression lines give initial $\delta^{26}\text{Mg}^*$ values, $(\delta^{26}\text{Mg}^*)_0$, of $0.21 \pm 0.16\%$ for Y20-1X1 and $-0.01 \pm 0.54\%$ for Y20-9-1. The $\delta^{26}\text{Mg}^*$ values of the diopside rim in Y20-1X1 plot slightly lower than the regression line defined by melilite and spinel in this CAI (Fig. 4a). The average $\delta^{26}\text{Mg}^*$ value of the diopside rim of this CAI is $-0.07 \pm 0.06\%$ (2SE, N = 7), which is resolvable from the intercept of the melilite-spinel regression line $[(\delta^{26}\text{Mg}^*)_0 = 0.21 \pm 0.16\%]$. Including the data for melilite, spinel, and the diopside rim of Y20-1X1 gives $(^{26}\text{Al}/^{27}\text{Al})_0 = (5.3 \pm 0.3) \times 10^{-5}$ (MSWD = 0.9) and $(\delta^{26}\text{Mg}^*)_0 = -0.01 \pm 0.08\%$.

Minerals in the two CAIs show variations in $\delta^{25}\text{Mg}_{\text{DSM-3}}$ values $(-2.1 \leq \delta^{25}\text{Mg}_{\text{DSM-3}} \leq 4.9$; Table 1). Melilite and spinel in Y20-1X1 exhibit positive $\delta^{25}\text{Mg}_{\text{DSM-3}}$ values $(2.5 \leq \delta^{25}\text{Mg}_{\text{DSM-3}} \leq 4.9$; Fig. 5), while the diopside rim exhibits negative $\delta^{25}\text{Mg}_{\text{DSM-3}}$ values $(-2.1 \leq \delta^{25}\text{Mg}_{\text{DSM-3}} \leq -0.1$; Fig. 5). In contrast to melilite in Y20-1X1, melilite in Y20-9-1 does not show significant mass-dependent isotopic fractionation in Mg isotopes $(-1.0 \leq \delta^{25}\text{Mg}_{\text{DSM-3}} \leq 0.6$; Fig. 5) from the chondritic Mg isotope ratio $(\delta^{25}\text{Mg}_{\text{DSM-3}} = -0.15 \pm 0.04\%$, 2SD; Teng et al., 2010).

3.3. Li-Be-B isotope systematics

Fig. 6a shows a change of $^{11}\text{B}^+ / ^{30}\text{Si}^+$ ratios during sample measurements, indicating that the $^{11}\text{B}^+ / ^{30}\text{Si}^+$ ratios were stable during individual analyses for ~ 70 min (e.g., melilite #10 in Fig. 6a). This demonstrates that surface contamination has been removed by the presputtering under the condition described in Section 2.4, otherwise we may see a monotonic decrease of the $^{11}\text{B}^+ / ^{30}\text{Si}^+$ ratio at the beginning of the analysis (Fujiya et al., 2016). Some analyses showed an increase of the $^{11}\text{B}^+ / ^{30}\text{Si}^+$ ratios in the middle of the analysis (e.g., melilite #3 in Fig. 6a), which may result from the sputtering of B-rich phase(s) other than melilite. Thus, these measurement cycles were excluded for summing up signals. Fig. 6b shows $^9\text{Be}/^{11}\text{B}$ and $^{10}\text{B}/^{11}\text{B}$ ratios calculated from a single analysis of melilite in CAI Y20-9-1 (melilite #10), individuals of which were obtained by summing up signals from different depths (i.e., every 50 cycles within the total 200 cycle analysis). We do not find any resolvable changes in $^9\text{Be}/^{11}\text{B}$ and $^{10}\text{B}/^{11}\text{B}$ ratios at each depth, supporting that the presputtering successfully removed the surface contamination.

The Li, Be, and B concentrations, $^9\text{Be}/^{11}\text{B}$, $^{10}\text{B}/^{11}\text{B}$, and $^7\text{Li}/^6\text{Li}$ ratios of measured CAI minerals are given in Table 2. The $^{10}\text{B}/^{11}\text{B}$ ratios as functions of $^9\text{Be}/^{11}\text{B}$ and $1/[\text{B} \text{ (ppm)}]$ of CAI minerals are shown in Fig. 7. Melilite in the two CAIs shows large variations in $^{10}\text{B}/^{11}\text{B}$ ratios ranging from 0.34 ± 0.05 (2σ) to 1.31 ± 0.36 (2σ), all of

which are higher than the chondritic B isotopic composition ($^{10}\text{B}/^{11}\text{B} = 0.2481$; Zhai et al., 1996). The corresponding $\delta^{10}\text{B}$ values (where $\delta^{10}\text{B} = [(^{10}\text{B}/^{11}\text{B})_{\text{sample}} / (^{10}\text{B}/^{11}\text{B})_{\text{NIST SRM 951-1}} - 1] \times 1000$) range from $370 \pm 60\%$ (2σ) to $4300 \pm 1200\%$ (2σ). The B isotope ratios of melilite are positively correlated with the corresponding $^9\text{Be}/^{11}\text{B}$ ratios ranging from 19 ± 2 (2σ) to 335 ± 74 (2σ) (Fig. 7a-b). The observed correlations are better than correlations between the B isotopic ratios and $1/[\text{B} \text{ (ppm)}]$ (Fig. 7c-d), in favor of in situ decay of ^{10}Be rather than mixing lines. The regressions in Fig. 7 were performed using Isoplot 4.15 (model 1, Ludwig, 2012). Uncertainties in initial $^{10}\text{Be}/^9\text{Be}$ ratios and initial $^{10}\text{B}/^{11}\text{B}$ ratios are 95% confidence limits. The inferred initial $^{10}\text{Be}/^9\text{Be}$ ratios, $(^{10}\text{Be}/^9\text{Be})_0$, of Y20-1X1 and Y20-9-1 are $(2.9 \pm 0.6) \times 10^{-3}$ (MSWD = 1.2) and $(2.2 \pm 1.0) \times 10^{-3}$ (MSWD = 2.5), respectively. The initial $^{10}\text{B}/^{11}\text{B}$ ratios, $(^{10}\text{B}/^{11}\text{B})_0$, are determined to be 0.256 ± 0.059 for Y20-1X1 and 0.269 ± 0.093 for Y20-9-1, which are indistinguishable from the chondritic B isotopic composition ($^{10}\text{B}/^{11}\text{B} = 0.2481$). Note that these $(^{10}\text{Be}/^9\text{Be})_0$ and $(^{10}\text{B}/^{11}\text{B})_0$ values are calculated using the data for melilite only. For CAI Y20-1X1, we also analyzed the diopside rim. The $^{10}\text{B}/^{11}\text{B}$ and $^9\text{Be}/^{11}\text{B}$ ratios of the diopside rim are 0.251 ± 0.004 (2σ) and 0.011 ± 0.001 (2σ), respectively. Including the diopside data, we obtain $(^{10}\text{Be}/^9\text{Be})_0 = (3.0 \pm 0.4) \times 10^{-3}$ (MSWD = 1.05) and $(^{10}\text{B}/^{11}\text{B})_0 = 0.251 \pm 0.004$, both of which are consistent with the regression for melilite only.

Three Li isotope measurements of melilites (one for Y20-1X1 and the other two for Y20-9-1) yield $^7\text{Li}/^6\text{Li} = 12.2 \pm 0.2$ (2σ), 12.1 ± 0.4 (2σ), and 12.0 ± 0.4 (2σ), which are identical with the chondritic Li isotopic composition ($^7\text{Li}/^6\text{Li} = 12.06$; Seitz et al., 2007) within uncertainties. The Li concentration of melilite from Y20-1X1 is 630 ± 82 (ppb, 2σ), which is one order of magnitude higher than those of melilites from Y20-9-1 (59–71 ppb).

4. DISCUSSION

4.1. Formation scenarios of the present CO CAIs inferred from REE and Al-Mg isotope systematics

Here we discuss possible formation scenarios of the two CO CAIs Y20-1X1 and Y20-9-1. In the following discussion, formation ages of these CAIs are determined by assuming a homogeneous distribution of ^{26}Al with the canonical $^{26}\text{Al}/^{27}\text{Al}$ ratio of 5.2×10^{-5} at the CAI-forming region. The bulk Al-Mg isochrons of CAIs from CV and CR chondrites yield well-defined $^{26}\text{Al}/^{27}\text{Al}$ slopes of $\sim 5.1\text{--}5.2 \times 10^{-5}$ (Jacobsen et al., 2008; Larsen et al., 2011, 2020), indicating that at least CV and CR CAI-forming regions might have been significantly homogenized for ^{26}Al abundance. There are no bulk Al-Mg data of CAIs from CO chondrites, while multi-CAI isochrons for CO CAIs indicate that they have formed from reservoir(s) with initial $^{26}\text{Al}/^{27}\text{Al}$ ratios of $\sim 4.9\text{--}5.4 \times 10^{-5}$ (Liu et al., 2019). These data suggest that ^{26}Al heterogeneity of ^{26}Al -bearing CAI-forming regions would have been within 10% of the canonical value. If the initial $^{26}\text{Al}/^{27}\text{Al}$ ratios of CO CAI-forming regions were 10% more/less than those of CV

Table 1
The Al-Mg isotope data of melilite, spinel, and diopside in CAIs from Yamato-81020.

Minerals/Analysis location#	$\delta^{25}\text{Mg}_{\text{DSM-3}}$ (‰)	2 σ	$^{27}\text{Al}/^{24}\text{Mg}$	2 σ	$\delta^{26}\text{Mg}^*$ (‰)	2 σ	Minerals/Analysis location#	$\delta^{25}\text{Mg}_{\text{DSM-3}}$ (‰)	2 σ	$^{27}\text{Al}/^{24}\text{Mg}$	2 σ	$\delta^{26}\text{Mg}^*$ (‰)	2 σ
<i>Y20-9-1</i>							<i>Y20-1X1</i>						
melilite #1	-0.72	0.41	30.79	0.48	10.27	0.60	melilite #1	2.90	0.30	8.21	0.14	2.95	0.27
melilite #3	-0.85	0.41	27.07	0.31	9.43	0.48	melilite #2	3.08	0.30	4.95	0.06	1.93	0.27
melilite #4	-0.21	0.37	37.36	0.39	13.85	0.60	melilite #3	3.30	0.30	7.28	0.09	2.70	0.27
melilite #5	0.61	0.30	28.18	0.36	9.42	0.51	melilite #4	2.99	0.30	4.36	0.08	1.73	0.27
melilite #6	0.23	0.42	36.63	0.44	12.59	0.68	melilite #5	2.95	0.30	1.89	0.02	0.88	0.27
melilite #7	0.30	0.41	26.92	0.32	9.57	0.48	melilite #6	2.83	0.30	4.77	0.06	1.87	0.27
melilite #8	-0.06	0.33	37.41	0.47	13.60	0.57	melilite #7	2.51	0.30	5.84	0.10	2.21	0.27
melilite #9	0.13	0.28	40.61	0.53	14.46	0.61	melilite #8	2.45	0.30	6.05	0.15	2.26	0.27
melilite #10	0.10	0.29	27.03	0.28	9.76	0.56	spinel #1	3.22	0.23	2.56	0.03	1.15	0.21
melilite #11	0.32	0.32	26.18	0.28	9.13	0.65	spinel #2	4.87	0.23	2.55	0.03	1.09	0.18
melilite #12	0.02	0.42	31.23	0.36	10.51	0.56	spinel #3	4.74	0.23	2.55	0.03	0.98	0.16
melilite #13	-0.16	0.41	21.90	0.26	7.83	0.38	diopside #1	-2.15	0.31	0.057	0.001	0.10	0.26
melilite #14	-0.07	0.37	30.95	0.38	11.23	0.51	diopside #2	-0.26	0.31	0.151	0.009	-0.03	0.26
melilite #15	-0.98	0.37	30.17	0.43	10.61	0.57	diopside #3	-0.27	0.31	0.046	0.001	-0.12	0.26
melilite #16	0.45	0.37	16.04	0.18	5.73	0.40	diopside #4	-1.47	0.31	0.043	0.001	-0.10	0.26
melilite #18	0.55	0.37	26.93	0.72	9.48	0.47	diopside #5	-0.30	0.31	0.048	0.001	-0.12	0.26
melilite #24	0.35	0.37	31.04	0.36	11.15	0.57	diopside #6	-0.07	0.31	0.074	0.002	-0.07	0.26
melilite #25	0.31	0.37	29.06	0.41	10.25	0.49	diopside #7	-1.66	0.31	0.050	0.002	-0.11	0.26
melilite #27	0.63	0.48	43.71	0.88	14.87	0.83							
melilite #28	0.34	0.39	20.37	0.22	7.22	0.57							

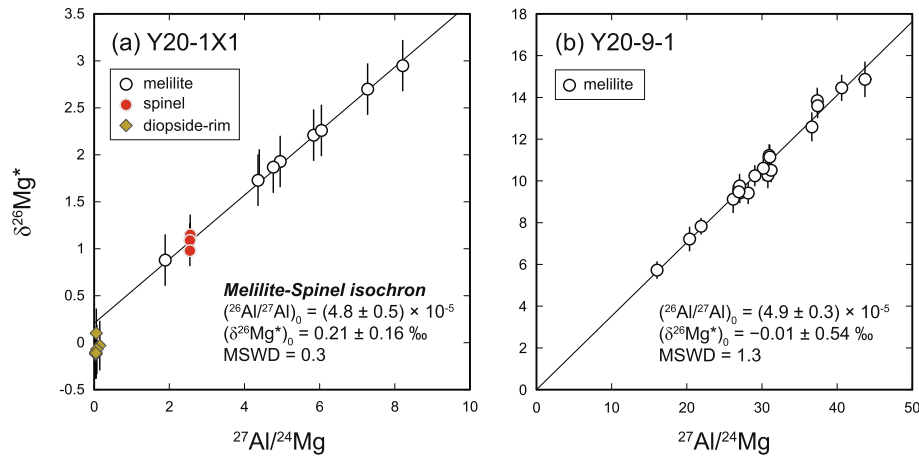


Fig. 4. ^{26}Al - ^{26}Mg isochron diagrams for (a) Y20-1X1 and (b) Y20-9-1 from Yamato-81020 (CO3.05) chondrite. For Y20-1X1, data for diopside-rim were not included in the regression to determine the $(^{26}\text{Al}/^{27}\text{Al})_0$ and $(\delta^{26}\text{Mg}^*)_0$ (see Section 4.1.1 for more discussion). Error bars are 2σ . Uncertainties in $(^{26}\text{Al}/^{27}\text{Al})_0$ and $(\delta^{26}\text{Mg}^*)_0$ are 95% confidence limits.

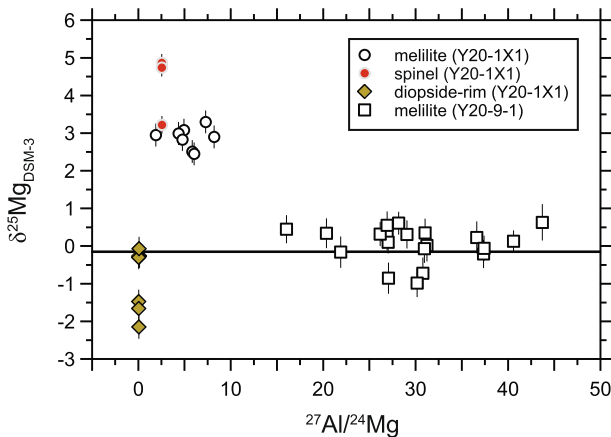


Fig. 5. Relationships between $\delta^{25}\text{Mg}_{\text{DSM-3}}$ (‰) and $^{27}\text{Al}/^{24}\text{Mg}$ ratios of individual Al-Mg isotope analyses for two CAIs (Y20-1X1 and Y20-9-1) from Yamato-81020 (CO3.05) chondrite. A solid line represents the chondritic $\delta^{25}\text{Mg}_{\text{DSM-3}}$ value ($\delta^{25}\text{Mg}_{\text{DSM-3}} = -0.15 \pm 0.04\text{‰}$, 2SD; Teng et al., 2010). Error bars are 2σ . Note that $\delta^{25}\text{Mg}_{\text{DSM-3}}$ values of spinel (closed circle symbols) are calculated by assuming the $\delta^{25}\text{Mg}_{\text{DSM-3}}$ value of spinel standard to be 0 (see Section 2.3) so that these values would be systematically offset from true values.

and CR CAI-forming regions, then the relative formation ages of Y20-1X1 and Y20-9-1 would have been under/over-estimated by 0.1 Myr. Note, however, that distribution of ^{26}Al was not completely homogeneous at least during an epoch of formation of refractory inclusions because of the presence of ^{26}Al -poor refractory solids that were likely formed prior to injection and/or homogenization of ^{26}Al in the solar protoplanetary disk (Sahijpal and Goswami, 1998; Krot et al., 2012, 2019 and references therein; Makide et al., 2013; Holst et al., 2013; Kööp et al., 2016, 2018; Park et al., 2017 and references therein). Thus, we cannot rule out the possibility of heterogeneous distribution of ^{26}Al at the CO CAI-forming region. If this is the case, our Al-Mg data suggest that the present CO CAIs formed

in a similar reservoir to that for CV and CR CAIs since $(^{26}\text{Al}/^{27}\text{Al})_0$ values of the present CO CAIs are not resolvable from the canonical value.

4.1.1. Y20-1X1

A perovskite-rich region and melilite in Y20-1X1 show similar REE abundance patterns with depletions in ultra-refractory HREEs (Gd to Er and Lu) relative to light REEs (LREEs; La to Sm) (Fig. 3), which are a Group II-like REE pattern (Martin and Mason, 1974; Boynton, 1975; Davis and Grossman, 1979). The former shows ~ 10 – 100 times higher REE abundances than the latter, while Eu in the latter exhibits a large enrichment relative to other REEs. Repeated analyses confirmed that these characteristics are reproducible (Fig. A1a in Electronic Annex EA2). The higher REE abundances in perovskite-rich regions than melilite, as well as Eu-enrichment in melilite, are best explained by equilibrium partitioning among minerals crystallized from a melt (e.g., Nagasawa et al., 1980). These observations are consistent with the rounded shape of this CAI, suggesting that it was once molten. However, the Group II-like REE pattern cannot be produced by fractionation during melting, but only by condensation from a fractionated gas previously depleted in ultra-refractory HREEs (Martin and Mason, 1974; Boynton, 1975; Davis and Grossman, 1979). Thus, the observed Group II-like REE pattern suggests that its precursor has formed directly by condensation from the solar nebula. Small positive anomalies in Ce and Yb (possibly not in Eu) indicate further condensation of these less-refractory REEs onto the precursor with the Group II REE pattern (Hiyagon et al., 2011). Finally, the precursor with the Group II-like REE pattern would have experienced melting and recrystallization from the melt, resulting in the higher REE abundances in perovskite-rich regions than melilite, as well as Eu-enrichment in melilite.

The Mg stable isotope ratios of melilite and spinel in Y20-1X1 are positively fractionated (~ 2.5 – 4.9‰ in $\delta^{25}\text{Mg}_{\text{DSM-3}}$), which could result from melting of their precursor

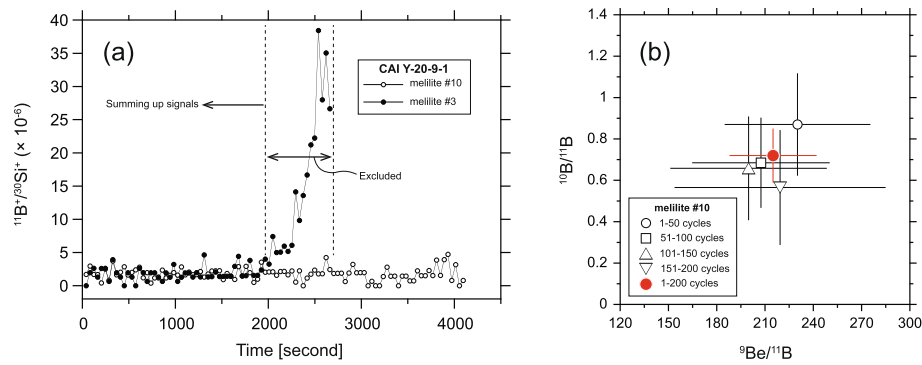


Fig. 6. Examples of Be-B isotope analyses of melilite in CAI Y20-9-1 from Yamato-81020 (CO3.05) chondrite. (a) Change in the $^{11}\text{B}^+ / ^{30}\text{Si}^+$ ratios during individual analyses (analysis spots #3 and #10). Most analyses show nearly-constant $^{11}\text{B}^+ / ^{30}\text{Si}^+$ ratio during the analyses with the duration of up to 70 min (=200 cycles; e.g., melilite #10). Some analyses show significant change in the $^{11}\text{B}^+ / ^{30}\text{Si}^+$ ratios during the analysis (e.g., melilite #3). Considering that the elevated ratios result from the sputtering of B-rich phase(s) other than melilite, these cycles were excluded for summing up signals to calculate the Be and B abundances and $^{10}\text{B} / ^{11}\text{B}$ and $^9\text{Be} / ^{11}\text{B}$ ratios. (b) $^{10}\text{B} / ^{11}\text{B}$ and $^9\text{Be} / ^{11}\text{B}$ ratios of different depths calculated from single analysis (200 cycles in total; melilite #10) that were divided into four sections with each 50 cycle. Instrumental mass fractionation and relative sensitivity were corrected for each section using the NIST SRM 610. The final values that were calculated by summing up all signals are also shown as a closed circle symbol. Error bars are 2σ .

Table 2
The Li-Be-B isotope data of melilite and diopside in CAIs from Yamato-81020.

Minerals/Analysis location#	Li (ppb)	2σ	$^7\text{Li} / ^6\text{Li}$	2σ	Be (ppb)	2σ	B (ppb)	2σ	$^9\text{Be} / ^{11}\text{B}$	2σ	$^{10}\text{B} / ^{11}\text{B}$	2σ
<i>Y20-1X1</i>												
melilite #1					529	29	28	2	30	3	0.338	0.052
melilite #2					648	14	15	2	78	9	0.470	0.094
melilite #3					736	48	7	1	267	40	1.058	0.209
melilite #4					578	38	5	1	251	37	0.998	0.198
melilite #5					563	37	7	1	161	19	0.695	0.118
melilite #7					763	50	9	1	162	19	0.666	0.110
melilite #8					555	37	14	2	80	12	0.666	0.150
melilite #9					550	36	7	1	178	24	0.843	0.154
diopside-rim #6					22	1	2912	115	0.011	0.001	0.251	0.004
melilite #10	630	82	12.2	0.2								
<i>Y20-9-1</i>												
melilite #1					909	80	12	2	157	30	0.820	0.217
melilite #2					800	71	68	5	19	2	0.338	0.048
melilite #3					843	75	7	1	335	74	1.309	0.365
melilite #5					733	50	6	1	332	72	1.160	0.321
melilite #6					892	61	12	1	131	15	0.458	0.074
melilite #8					662	45	18	2	59	7	0.358	0.073
melilite #9					787	52	15	1	94	11	0.494	0.086
melilite #10					714	47	7	1	215	27	0.723	0.127
melilite #11	71	9	12.1	0.4								
melilite #12	59	8	12.0	0.4								

solids in the solar nebula and evaporation of Mg from the melt. The $^{27}\text{Al} / ^{24}\text{Mg}$ ratios and $\delta^{26}\text{Mg}^*$ values of melilite and spinel in Y20-1X1 form the well-defined single isochron (Fig. 4a) with $(^{26}\text{Al} / ^{27}\text{Al})_0 = (4.8 \pm 0.5) \times 10^{-5}$, indicative of the contemporaneous formation of the melilite and spinel, that is, co-crystallization from an isotopically fractionated melt. In contrast, the Al-Mg isotope data of diopside rim in Y20-1X1 do not plot on the melilite-spinel isochron (Fig. 4a). Furthermore, $\delta^{25}\text{Mg}_{\text{DSM-3}}$ values of diopside are consistently negative (-2.1 to -0.1% ; Fig. 5), suggesting its formation by condensation from the solar nebula

(Richter, 2004). The distinct magnitudes of Mg isotope fractionation between CAI interior and its rim have been observed in CAIs from CV chondrites (Simon et al., 2005; Kawasaki et al., 2019; Han et al., 2020). The Al-Mg isotope systematics of the CO CAI also indicate different origins of the core and rim.

The intercept of the melilite-spinel isochron of Y20-1X1 is $(\delta^{26}\text{Mg}^*)_0 = 0.21 \pm 0.16\%$, which is slightly higher than the inferred Solar System initial values (-0.040% ; Jacobsen et al., 2008, or -0.016% ; Larsen et al., 2011). The observed $(\delta^{26}\text{Mg}^*)_0$ value can be understood as a result

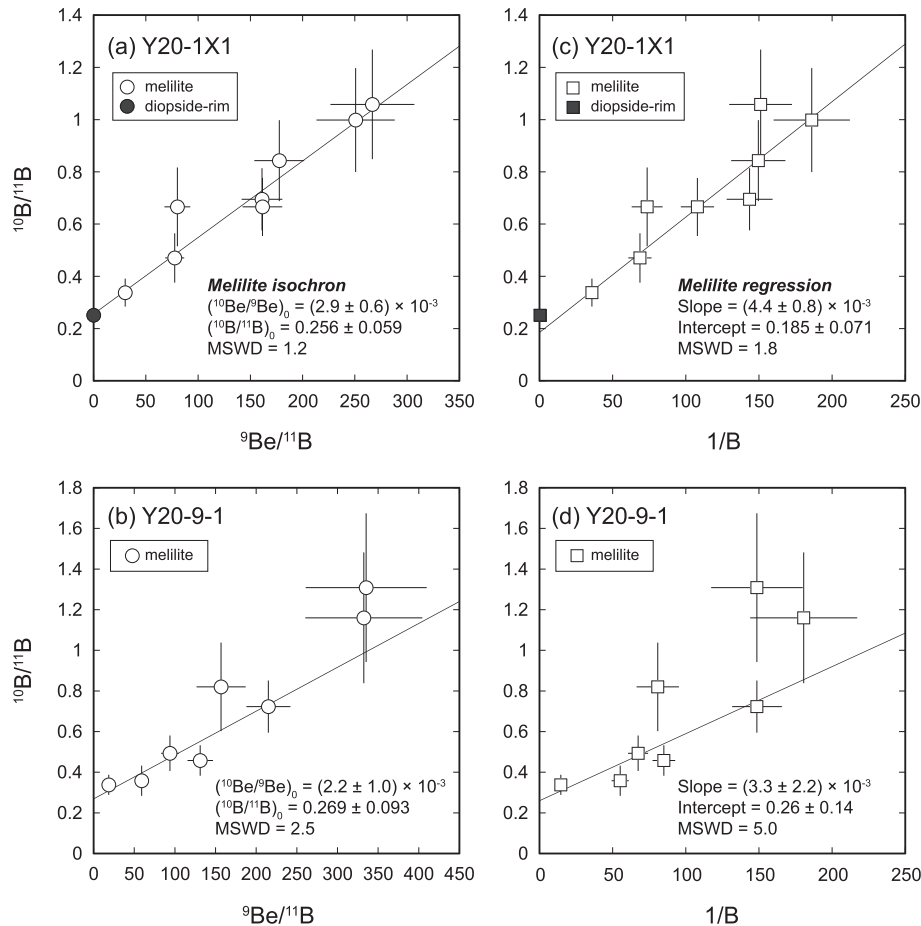


Fig. 7. ^{10}Be - ^{10}B isochron and $1/\text{B}$ (ppm) versus $^{10}\text{B}/^{11}\text{B}$ diagrams for (a, c) Y20-1X1 and (b, d) Y20-9-1 from Yamato-81020 (CO3.05) chondrite. Data for diopside-rim (closed symbols) were not included in the regressions for Y20-1X1 (a and c). For both CAIs, MSWD values of the isochron regressions (a and b) are smaller than those for $1/\text{B}$ versus $^{10}\text{B}/^{11}\text{B}$ (c and d), indicating that variations in B isotope ratios resulted from the in situ decay of ^{10}Be . Error bars are 2σ . Uncertainties in the slopes and intercepts are 95% confidence limits.

of Mg isotopic evolution due to the decay of ^{26}Al to ^{26}Mg within its precursor material. On the basis of the relationship between $(^{26}\text{Al}/^{27}\text{Al})_0$ and $(\delta^{26}\text{Mg}^*)_0$ values obtained from Al-Mg mineral isochron data, the timing of the final bulk Al/Mg fractionation event can be calculated (e.g., MacPherson et al., 2012). As shown in Fig. 8, the observed $(\delta^{26}\text{Mg}^*)_0$ value of Y20-1X1 can be understood as a result of Mg isotopic evolution of a precursor material with $^{27}\text{Al}/^{24}\text{Mg}$ ratio > 3 , which is consistent with the estimated present bulk $^{27}\text{Al}/^{24}\text{Mg}$ ratio (~ 3.2) based on the modal abundances and average chemical compositions of melilite and spinel (Electronic Annex EA2). Thus, the Al-Mg isotope systematics of melilite and spinel are readily explained by thermal processing of precursor solids that have formed with $^{27}\text{Al}/^{24}\text{Mg} = \sim 3.2$ and canonical $(^{26}\text{Al}/^{27}\text{Al})_0$. Of note, we do not take into account the diopside rim for the estimation of the bulk $^{27}\text{Al}/^{24}\text{Mg}$ ratio considering that the rim condensed directly from the solar nebula. The $(^{26}\text{Al}/^{27}\text{Al})_0$ of Y20-1X1 is $(4.8 \pm 0.5) \times 10^{-5}$, corresponding to an age difference of $0.1^{-0.10}/_{+0.11}$ Myr relative to the canonical $(^{26}\text{Al}/^{27}\text{Al})_0$. Therefore, this thermal processing could have occurred within ~ 0.2 Myr after the formation of the precursor solids. Note, however, that melilite and spinel show

positive $\delta^{25}\text{Mg}_{\text{DSM-3}}$ values. This suggests that some amounts of Mg were evaporated from a CAI melt, assuming the chondritic Mg isotopic composition of its precursors. Since the precise $\delta^{25}\text{Mg}_{\text{DSM-3}}$ value for spinel standard was not available at present (see Section 2.3), however, the obtained $\delta^{25}\text{Mg}_{\text{DSM-3}}$ values for spinel in Y20-1X1 may be systematically offset from the true values. Therefore, we only discuss the $\delta^{25}\text{Mg}_{\text{DSM-3}}$ values for melilite (2.9‰ on average). Richter et al. (2007) conducted evaporation experiments with a type B CAI-like material and investigated a relationship between elemental and Mg isotope fractionation, showing that $\sim 20\%$ loss of Mg would induce isotope fractionation in 2.9‰/amu from the CAI melt. Therefore, if the Mg isotope fractionation occurred at the final melting of Y20-1X1, the precursors of this CAI would have more Mg-rich bulk composition ($^{27}\text{Al}/^{24}\text{Mg} \sim 2.5$). If we adopt a $^{27}\text{Al}/^{24}\text{Mg}$ ratio of 2.5, then the $(\delta^{26}\text{Mg}^*)_0$ value of Y20-1X1 plots at marginally higher than the evolution curve (Fig. 8), suggesting that its precursors have not formed from gas with the chondritic Mg isotopic composition, but isotopically fractionated gas ($\delta^{25}\text{Mg}_{\text{DSM-3}} \sim 2.9\%$). Alternatively, this discrepancy may reflect either that our $^{27}\text{Al}/^{24}\text{Mg}$ estimate based on the two-dimensional

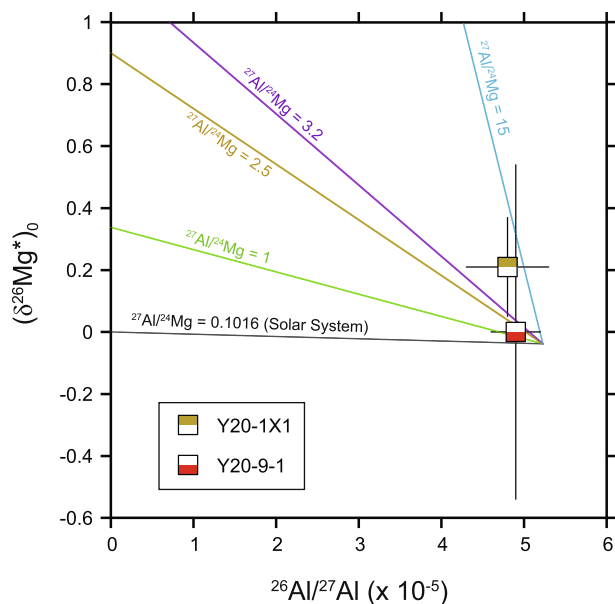


Fig. 8. Mg isotope evolution diagram for two CAIs (Y20-1X1 and Y20-9-1) from Yamato-81020 (CO3.05) chondrite. Growth curves of $\delta^{26}\text{Mg}^*$ as a function of time are also shown for hypothetical reservoirs with different $^{27}\text{Al}/^{24}\text{Mg}$ ratios. The curve for the bulk Solar System reservoir ($^{27}\text{Al}/^{24}\text{Mg} = 0.1016$; Lodders, 2003) is shown in black. For each evolution curve, the initial $^{26}\text{Al}/^{27}\text{Al}$ ratio and $(\delta^{26}\text{Mg}^*)_0$ value at time “zero” are assumed to be 5.23×10^{-5} and -0.040‰ , respectively (Jacobsen et al., 2008). Note that the $(\delta^{26}\text{Mg}^*)_0$ and initial $^{26}\text{Al}/^{27}\text{Al}$ ratio of Y20-1X1 are obtained from the melilite-spinel isochron, not including data for diopside-rim (see Section 4.1.1). Data for Y20-1X1 plots slightly higher than expected bulk $^{27}\text{Al}/^{24}\text{Mg}$ ratios ($^{27}\text{Al}/^{24}\text{Mg} = \sim 2.5\text{--}3.2$), but consistent with the Mg isotope evolution of a precursor with $^{27}\text{Al}/^{24}\text{Mg} = 3.2$ within uncertainties (see more discussion in the Section 4.1.1). Uncertainties are 95% confidence limits.

elemental mapping is inaccurate and/or that the experimental results for type B CAI-like materials cannot be directly applied to the present CAI Y20-1X1. Note that the pre-evaporation bulk $^{27}\text{Al}/^{24}\text{Mg}$ ratio = 2.5 was estimated assuming that evaporated Mg was not back-condensed onto the CAI. If this assumption is invalid, the estimated evaporative loss of Mg ($\sim 20\%$) would be underestimated (Nagahara and Ozawa, 2000), meaning that the true value is even lower than the estimated value. In this case, the discrepancy between the $(\delta^{26}\text{Mg}^*)_0$ value of Y20-1X1 and the expected evolution curve would be more significant.

Overall, the REE and Al-Mg isotope systematics of Y20-1X1 suggest that this CAI formed by melting of CAI-like precursor solids that have been condensed from the solar nebula and its diopside rim has subsequently formed by condensation from the solar nebula. Hence, we deduced the $(^{10}\text{Be}/^9\text{Be})_0$ and $(^{10}\text{B}/^{11}\text{B})_0$ values for this CAI from the melilite data only, and the diopside rim data will not be included in the following discussion.

4.1.2. Y20-9-1

Melilite in Y20-9-1 also shows a group II-like REE pattern (Fig. 3 and Fig. A1b in Electronic Annex EA2), suggesting the condensation of this CAI or its precursor

from a fractionated gas. Some melilite grains show negative $\delta^{25}\text{Mg}_{\text{DSM-3}}$ values down to $-1.0 \pm 0.4\text{‰}$ (2σ ; Fig. 5). The negative $\delta^{25}\text{Mg}_{\text{DSM-3}}$ values are often observed in amoeboid olivine aggregates (Larsen et al., 2011; Olsen et al., 2011; MacPherson et al., 2012; Fukuda et al., 2021) that are thought to be aggregates of solids condensed from the solar nebula (e.g., Krot et al., 2004). The negative $\delta^{25}\text{Mg}_{\text{DSM-3}}$ values of some melilite grains also indicate that this CAI has condensed from the solar nebula, and not experienced significant melting after their condensation. The $(^{26}\text{Al}/^{27}\text{Al})_0$ value of Y20-9-1 is $(4.9 \pm 0.3) \times 10^{-5}$, corresponding to an age difference of $0.06^{+0.06}/_{-0.05}$ Myr relative to the canonical value. The intercept of the melilite isochron is $(\delta^{26}\text{Mg}^*)_0 = -0.01 \pm 0.54\text{‰}$, which is not resolvable from the inferred Solar System initial values. Although the uncertainty of $(\delta^{26}\text{Mg}^*)_0$ is not small enough to discuss the Mg isotopic evolution precisely (Fig. 8), the unresolvable $(\delta^{26}\text{Mg}^*)_0$ value does not conflict with its condensation from the Solar composition gas. However, Y20-9-1 shows positive anomalies in Ce, Eu, and Yb, suggesting that this CAI is not a single stage condensation product but contains later additional condensation component(s) of these most volatile REEs.

4.2. Initial abundances of ^{26}Al and ^{10}Be in CAIs and their implications for the origin of ^{10}Be in the early Solar System

Since the discovery of the former presence of ^{10}Be in CAIs (McKeegan et al., 2000), a possible correlation between ^{26}Al and ^{10}Be abundances in CAIs has been investigated to discuss the origins of these SLRs (Sugiura et al., 2001; Marhas et al., 2002; MacPherson et al., 2003; Chaussidon et al., 2006; Liu et al., 2009, 2010; Srinivasan and Chaussidon, 2013; Gounelle et al., 2013; Fukuda et al., 2019). Fig. 9 summarizes the inferred $(^{26}\text{Al}/^{27}\text{Al})_0$ and $(^{10}\text{Be}/^9\text{Be})_0$ values of the present CO CAIs and other CAIs from CV, CM, CH, and CH/CB chondrites (MacPherson et al., 2003; Chaussidon et al., 2006; Liu et al., 2009, 2010; Srinivasan and Chaussidon, 2013; Gounelle et al., 2013; Mishra and Marhas, 2019; Fukuda et al., 2019). Data from Sugiura et al. (2001) are not shown in Fig. 9, because most of their Al-Mg data were obtained from plagioclase analyses, which could have been disturbed by thermal metamorphism on the parent bodies (e.g., LaTourrette and Wasserburg, 1998; MacPherson et al., 2012; Van Orman et al., 2014). No obvious correlation between the $(^{26}\text{Al}/^{27}\text{Al})_0$ and $(^{10}\text{Be}/^9\text{Be})_0$ among CAIs can be observed (Fig. 9). The $(^{26}\text{Al}/^{27}\text{Al})_0$ values of the present CO CAIs are indistinguishable from the canonical value of 5.2×10^{-5} and are also within the range of those of CV CAIs (e.g., MacPherson et al., 2010, 2012; Kita et al., 2012; Srinivasan and Chaussidon, 2013; Mishra and Chaussidon, 2014; Kawasaki et al., 2017, 2018, 2019, 2020). In contrast, $(^{10}\text{Be}/^9\text{Be})_0$ values of the present CO CAIs ($2.9 \pm 0.6 \times 10^{-3}$ and $2.2 \pm 1.0 \times 10^{-3}$) are significantly higher than the average $(^{10}\text{Be}/^9\text{Be})_0$ value of CV CAIs ($\sim 0.7 \times 10^{-3}$) (Fig. 9). To date, the lowest $(^{10}\text{Be}/^9\text{Be})_0$ value for CAIs with near-canonical $(^{26}\text{Al}/^{27}\text{Al})_0 = \sim 4\text{--}5 \times 10^{-5}$ (hereafter ^{26}Al -rich CAIs) is $(4.8 \pm 1.7) \times 10^{-4}$ (MacPherson et al., 2003). Hence, the variation in

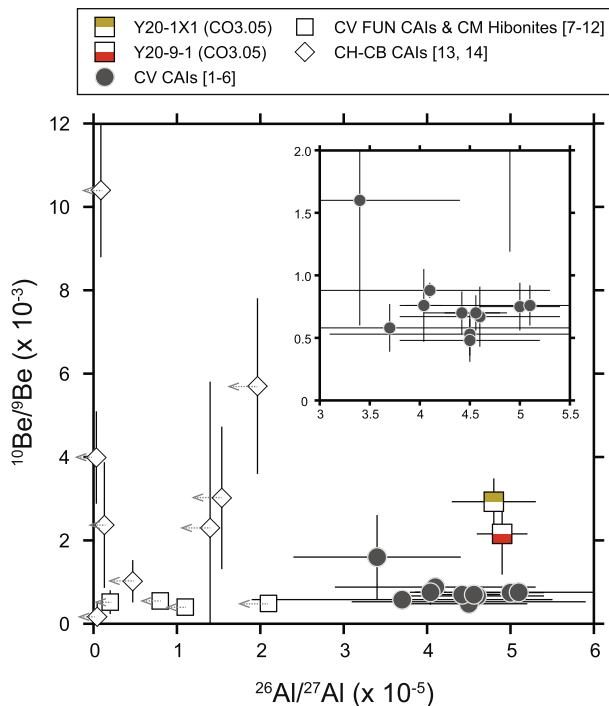


Fig. 9. Initial $^{10}\text{Be}/^9\text{Be}$ versus initial $^{26}\text{Al}/^{27}\text{Al}$ ratios of CAIs from various types of chondrites, CO CAIs (Y20-1X1 and Y20-9-1; this study), ^{26}Al -rich CV CAIs ([1] Podosek et al., 1991; [2] Goswami et al., 1994; [3] MacPherson et al., 2003; [4] Chaussidon et al., 2006; [5] Srinivasan and Chaussidon, 2013; [6] Mishra and Marhas, 2019), CV FUN CAIs and CM hibonites ([7] Srinivasan et al., 2000; [8] Marhas et al., 2002; [9] Thrane et al., 2008; [10, 11] Liu et al., 2009, 2010; [12] Wielandt et al., 2012), and CH-CB CAIs ([13] Gounelle et al., 2013; [14] Fukuda et al., 2019). For data reported in Gounelle et al. (2013), only data for CAI 411 is shown. Data for Wielandt et al. (2012) were recalculated using the relative sensitivity factor of NIST 612 (see Fukuda et al., 2018 for more details). The inset shows detail of ^{26}Al -rich CV CAIs. Note that only upper limits (2σ) for $^{26}\text{Al}/^{27}\text{Al}$ ratios are shown for CV FUN CAIs, CM hibonites, and CH-CB CAIs by arrows. Error bars are 2σ or 95% confidence limits.

($^{10}\text{Be}/^9\text{Be}$)₀ among the ^{26}Al -rich CAI forming-region(s) must be greater than a factor of six. The apparent variation in ($^{10}\text{Be}/^9\text{Be}$)₀ values among ^{26}Al -rich CAIs provides evidence for heterogeneous distribution of ^{10}Be at the time of ^{26}Al -rich CAI formation and argues against a homogeneous distribution of ^{10}Be expected for its molecular cloud origin (Desch et al., 2004; Dunham et al., 2019).

Recently, Fukuda et al. (2019) revisited the origin of ^{10}Be in the early Solar System based on their new Be-B isotopic analyses on CAIs in CH and CH/CB chondrites (hereafter CH-CB CAIs). They observed high and variable ($^{10}\text{Be}/^9\text{Be}$)₀ values ($0.17\text{--}6.1 \times 10^{-3}$) in CH-CB CAIs, and concluded that ^{10}Be was produced locally in the solar protoplanetary disk near the proto-Sun. This is because such high ($^{10}\text{Be}/^9\text{Be}$)₀ values ($>1 \times 10^{-3}$) are difficult to reconcile with models invoking inheritance of ^{10}Be from the presolar molecular cloud (Desch et al., 2004; Tatischeff et al., 2014) or neutrino spallation process in low-mass core-collapse supernovae (Banerjee et al., 2016). For the same reason,

the observed high ($^{10}\text{Be}/^9\text{Be}$)₀ values of the present CO CAIs also support the solar cosmic ray irradiation origin of ^{10}Be in the early Solar System (McKeegan et al., 2000; Gounelle et al., 2001, 2006, 2013; Goswami et al., 2001; MacPherson et al., 2003; Leya et al., 2003; Chaussidon et al., 2006; Liu et al., 2009, 2010; Bricker and Caffee, 2010; Wielandt et al., 2012; Srinivasan and Chaussidon, 2013; Sossi et al., 2017; Mishra and Marhas, 2019; Fukuda et al., 2019; Jacquet, 2019). Hence, the observed variation in ($^{10}\text{Be}/^9\text{Be}$)₀ values among the ^{26}Al -rich CAIs (Fig. 7) can be well understood as a result of heterogeneous, local production of ^{10}Be by cosmic ray irradiation caused by solar flares.

The solar cosmic ray irradiation origin of ^{10}Be is also consistent with the presence of ^7Be in CAIs from CV chondrites ($^7\text{Be}/^9\text{Be} = \sim 1\text{--}6 \times 10^{-3}$; Chaussidon et al., 2006; Mishra and Marhas, 2019). Because of its very short half-life ($T_{1/2} = 53$ days; Jaeger et al., 1996), ^7Be must be synthesized immediately before or after CAI formation, which argues against the inheritance of ^{10}Be from the molecular cloud (Desch et al., 2004) or low-mass core-collapse supernovae (Banerjee et al., 2016). In this study, we obtained Be-B and Li isotope data from different analytical spots so that our dataset cannot be used to discuss the possible presence of ^7Be in the present CO CAIs.

In solar cosmic ray irradiation models, one would expect that Li and B isotope ratios of an irradiation target are modified by spallation reactions alongside ^{10}Be production (e.g., Liu et al., 2010). In fact, some CAIs from CV chondrites show sub-chondritic $^7\text{Li}/^6\text{Li}$ ratios (MacPherson et al., 2003; Wielandt et al., 2012) and supra-chondritic initial $^{10}\text{B}/^{11}\text{B}$ ratios (Liu and Chaussidon, 2018 and references therein). Since the collateral effects on Li and B isotopes are highly dependent on the chemical compositions of irradiation targets (e.g., Chaussidon and Gounelle, 2006), the observed ($^{10}\text{Be}/^9\text{Be}$)₀, $^7\text{Li}/^6\text{Li}$, and initial $^{10}\text{B}/^{11}\text{B}$ ratios would constrain the nature of the irradiation targets, e.g., refractory solids or solar composition gas. The sub-chondritic $^7\text{Li}/^6\text{Li}$ and supra-chondritic initial $^{10}\text{B}/^{11}\text{B}$ ratios among some CV CAIs imply that a part of irradiation have taken place on the targets with elevated Be/Li and Be/B ratios relative to chondritic ones (Liu et al., 2010; Srinivasan and Chaussidon, 2013), which is consistent with the irradiation of CAI themselves. Given the level of their ($^{10}\text{Be}/^9\text{Be}$)₀ values ($\sim 4\text{--}10 \times 10^{-4}$) and chemical compositions, however, the observed $^7\text{Li}/^6\text{Li}$ and initial $^{10}\text{B}/^{11}\text{B}$ ratios among CV CAIs should be close to spallogenic $^7\text{Li}/^6\text{Li}$ (~ 0.8) and $^{10}\text{B}/^{11}\text{B}$ ($\sim 0.4\text{--}0.5$) ratios that are theoretically expected based on the spallation production ratios of Li and B (Yiou et al., 1968). In contrast, $^7\text{Li}/^6\text{Li}$ ($\sim 9\text{--}14.5$) and initial $^{10}\text{B}/^{11}\text{B}$ ratios ($\sim 0.235\text{--}0.258$) among CV CAIs are clearly different from the spallogenic $^{10}\text{B}/^{11}\text{B}$ and $^7\text{Li}/^6\text{Li}$ ratios (McKeegan et al., 2000; Sugiura et al., 2001; MacPherson et al., 2003; Chaussidon et al., 2006; Wielandt et al., 2012; Srinivasan and Chaussidon, 2013; Sossi et al., 2017; Mishra and Marhas, 2019). Therefore, if irradiation took place on the CAI themselves, additional mechanisms are required to explain the observed sub-chondritic $^7\text{Li}/^6\text{Li}$ and supra-chondritic initial $^{10}\text{B}/^{11}\text{B}$ ratios among CV CAIs, such as diffusive loss of

spallogenic Li and B (Liu et al., 2010) or mixing between spallogenic Li and B in refractory solids and the chondritic reservoir (e.g., solar composition gas) (Srinivasan and Chaussidon, 2013). In contrast, Fukuda et al. (2019) demonstrated that Li isotope ratios of CAIs from CH/CB chondrites are nearly chondritic, irrespective of their $(^{10}\text{Be}/^9\text{Be})_0$ values. These data can be readily explained by solar cosmic ray irradiation on a target with the chondritic Be/Li ratio of ~ 0.012 , but are inconsistent with a refractory target with elevated Be/Li ratio of ~ 10 . Although secondary modifications of Li isotope ratios by thermal processing in the solar nebula cannot be ruled out due to its high volatility and diffusivity (e.g., Srinivasan and Chaussidon, 2013), Fukuda et al. (2019) concluded that the irradiation targets were not solid CAI themselves but their precursors, possibly solar composition gas. In addition, there are also some CAIs from CV chondrites with sub-chondritic initial $^{10}\text{B}/^{11}\text{B}$ ratios (e.g., MacPherson et al., 2003). Considering both the supra- and sub-chondritic initial $^{10}\text{B}/^{11}\text{B}$ ratios among CV CAIs, it is possible that such a level of B isotopic heterogeneity existed at the CAI-forming regions.

Lithium isotope ratios and initial $^{10}\text{B}/^{11}\text{B}$ ratios of the present CO CAIs with high $(^{10}\text{Be}/^9\text{Be})_0$ values are identical to chondritic Li and B isotopic compositions within uncertainties, further supporting the conclusion by Fukuda et al. (2019). However, it should be noted that at least CAI Y20-1X1 would have experienced thermal processing of a CAI-like precursor (see Section 4.1.1 and Fig. 8), and therefore, its initial Li and B isotope ratios may have been lost during the thermal processing. Another CAI Y20-9-1 does not show evidence of significant melting after their condensation, which may retain its original Li-Be-B isotopic signatures. As noted earlier, however, because of the high volatility and diffusivity of Li, this is not conclusive. Since fine-grained CAIs tend to show a group II REE pattern, they are thought to be direct condensation products from the solar nebular and were unlikely melted (MacPherson, 2014 and references therein). In this case, these CAIs in the least metamorphosed chondrites may have preserved their initial Li and B isotopic signatures inherited from the solar nebula. Correlated studies on REE and Li-Be-B analyses of fine-grained CAIs will reveal more details of the nature of the irradiation targets.

As shown in Fig. 9, ^{26}Al -poor CAIs exhibit a large variation in $(^{10}\text{Be}/^9\text{Be})_0$ values (Marhas et al., 2002; MacPherson et al., 2003; Liu et al., 2009, 2010; Wielandt et al., 2012; Gounelle et al., 2013; Fukuda et al., 2019). Among them, $(^{10}\text{Be}/^9\text{Be})_0$ values of very refractory, ^{26}Al -poor CH-CB CAIs are highly variable (Gounelle et al., 2013; Fukuda et al., 2019). It has been proposed that very refractory, ^{26}Al -poor CH-CB CAIs formed at the very beginning of the Solar System, prior to injection and/or homogenization of ^{26}Al from a nearby star in the solar protoplanetary disk (e.g., Krot et al., 2008). If true, the high and variable $(^{10}\text{Be}/^9\text{Be})_0$ values of ^{26}Al -poor CH-CB CAIs would reflect fluctuations of energetic particle fluxes caused by episodic mass accretion events, such as FU-Ori outbursts (Fukuda et al., 2019). Note, however, that the other ^{26}Al -poor CAIs with large nucleosynthetic isotope anomalies,

such as CAIs with fractionation and unidentified nuclear effects (FUN CAIs; e.g., Wasserburg et al., 1977; Krot et al., 2014 and references therein; Park et al., 2017) in CV chondrites and platy hibonite crystals (PLACs; Ireland et al., 1988; Liu et al., 2009; Kööp et al., 2016) from the Murchison CM chondrite, tend to show consistently lower $(^{10}\text{Be}/^9\text{Be})_0$ values ($\sim 5 \times 10^{-4}$; Marhas et al., 2002; MacPherson et al., 2003; Liu et al., 2009, 2010; Wielandt et al., 2012). Because the large nucleosynthetic anomalies are not consistent with their late formation after the decay of ^{26}Al , these refractory solids are thought to have formed prior to injection and/or homogenization of ^{26}Al in the solar protoplanetary disk (e.g., Sahijpal and Goswami, 1998; Liu et al., 2009; Kööp et al., 2016, 2018). The $(^{10}\text{Be}/^9\text{Be})_0$ values of FUN CAIs and PLACs are within the range of those for ^{26}Al -poor CH-CB CAIs (Fig. 9), but the consistently lower $(^{10}\text{Be}/^9\text{Be})_0$ values would be inconsistent with the variable energetic particle fluxes caused by episodic accretion events. Tatischeff et al. (2014), therefore, concluded that the consistently lower $(^{10}\text{Be}/^9\text{Be})_0$ values for FUN CAIs and PLACs might not be derived from solar cosmic ray irradiation, but from irradiation of the presolar molecular cloud by freshly accelerated cosmic ray escaped from an isolated supernova remnant. Since ^{26}Al -poor CH-CB CAIs do not show large nucleosynthetic isotope anomalies (Kimura et al., 1993), the formation timings and/or locations of FUN CAIs and PLACs might be different from those of ^{26}Al -poor CH-CB CAIs. Combined Be-B and stable isotope studies (e.g., Ca and Ti) will provide an opportunity to better understand the origin of ^{10}Be among ^{26}Al -poor CAIs.

4.3. Irradiation conditions and implications for the astronomical settings of ^{26}Al -rich CAI formation

The newly obtained dataset in this study, together with the data of previous studies, reveal the apparent variations in $(^{10}\text{Be}/^9\text{Be})_0$ among the ^{26}Al -rich CAIs (Fig. 9). If ^{10}Be was produced by solar cosmic ray irradiation, the variation in $(^{10}\text{Be}/^9\text{Be})_0$ among CAIs are expected to reflect different irradiation conditions in the early solar nebula (e.g., proton fluence, chemical compositions of targets; Chaussidon and Gounelle, 2006 and references therein). On the basis of a model introduced by Fowler et al. (1962), the production ratio of ^{10}Be (relative to ^9Be) by solar cosmic ray irradiation can be written as

$$^{10}\text{Be}/^9\text{Be} = ^{16}\text{O}/^9\text{Be} \sum_i y_i \int \sigma_i(E) (dF/dE) dE$$

where y_i is the abundance of cosmic ray species ($i = ^3\text{He}$, ^4He) relative to proton ($y_p = 1$), $\sigma_i(E)$ is the cross section of a given nuclear reaction (cosmic ray + $^{16}\text{O} \rightarrow ^{10}\text{Be}$), and dF/dE is the proton differential fluence, F is the fluence, and E is the energy. If we assume $(dF/dE) = KE^{-\gamma}$ where the γ is the energy distribution spectral slope, $y_i = 0.1$ ($i = ^4\text{He}$), and use the cross sections of Gounelle et al. (2006), the estimated $^{10}\text{Be}/^9\text{Be}$ ratio is proportional to the chemical composition of the target (i.e., $^{16}\text{O}/^9\text{Be}$) and the proton fluence. Thus, by determining the chemical composition of target, the observed variation in $(^{10}\text{Be}/^9\text{Be})_0$ among the

^{26}Al -rich CAIs can be used to estimate a difference in the proton fluence. Considering the irradiation of CAI solid itself ($^{16}\text{O}/^9\text{Be} = 1.2 \times 10^7$), Gounelle et al. (2013) estimated the proton fluence that needed to account for the $(^{10}\text{Be}/^9\text{Be})_0 = 10.4 \times 10^{-3}$ observed in CAI 411 from CH/CB chondrite Isheyevo, which ranges from 1.7×10^{19} to 3.4×10^{20} protons cm^{-2} for γ varying between 2.5 and 4. Here we refer the estimation by Gounelle et al. (2013), but we consider the irradiation of solar composition gas (i.e., $^{16}\text{O}/^9\text{Be} = 3.4 \times 10^7$; Palme et al., 2014) instead of CAI solid itself. Using $(^{10}\text{Be}/^9\text{Be})_0 = (2.9 \pm 0.6) \times 10^{-3}$ for Y20-1X1 that was better constrained than that of Y20-9-1 [$(2.2 \pm 1.0) \times 10^{-3}$], we derive the proton fluences ranging from 1.7×10^{18} to 3.3×10^{19} protons cm^{-2} for γ varying between 2.5 and 4, while those for CV CAIs [$(^{10}\text{Be}/^9\text{Be})_0 = \sim 0.7 \times 10^{-3}$ in average] can also be calculated as 4.0×10^{17} to 8.1×10^{18} protons cm^{-2} for γ varying between 2.5 and 4.

The variation in the estimated proton fluences among ^{26}Al -rich CAIs can be understood as a difference in solar cosmic ray fluxes at their formation region. If all the ^{26}Al -rich CAIs formed at the same region and were irradiated by cosmic rays caused by solar flare having the similar spectral slope, one can expect that solar cosmic ray fluxes at the CAI-forming region would have fluctuated by at least a factor of six within a short duration (~ 0.2 Myr) that is inferred from the Al-Mg chronology. Alternatively, the variation in the estimated proton fluences among ^{26}Al -rich CAIs might reflect a difference in the formation locations of the CAIs (i.e., distance from the proto-Sun). Since energetic particle fluxes at inner parts of the protoplanetary disk were likely higher than at outer parts (e.g., Jacquet, 2019), the present CO CAIs could have formed closer to the Sun compared with ^{26}Al -rich CV CAIs (Fig. 10). Recently, Dunham et al. (2019) reported a weighted average $(^{10}\text{Be}/^9\text{Be})_0 = (8.4 \pm 1.6) \times 10^{-4}$ for six CO CAIs, which is clearly lower than $(^{10}\text{Be}/^9\text{Be})_0$ values of the present CO CAIs, but rather consistent with those for ^{26}Al -rich CV CAIs. By considering the data from Dunham et al.

(2019), the difference in $(^{10}\text{Be}/^9\text{Be})_0$ values among CO and CV CAIs is not related to the difference in their host chondrite groups (i.e., CV versus CO). Alternatively, it is possible that higher $(^{10}\text{Be}/^9\text{Be})_0$ values are related to their REE abundance patterns (Sossi et al., 2017). The higher $(^{10}\text{Be}/^9\text{Be})_0$ values recorded in the present CO CAIs with the group II REE pattern is consistent with the observation by Sossi et al. (2017), who demonstrated that the inferred $(^{10}\text{Be}/^9\text{Be})_0$ value for fine-grained CAIs with the group II REE pattern is higher than that for coarse-grained CAIs with an unfractionated REE pattern. These observations indicate that CAIs with the group II REE pattern (or at least their precursors) might have formed at inner parts of the solar protoplanetary disk (Fig. 10).

5. CONCLUSIONS

We have investigated Li-Be-B and Al-Mg isotope systematics and REE abundances in two CAIs, Y20-1X1 and Y20-9-1, from Y-81020 that is one of the least metamorphosed carbonaceous chondrites (CO3.05). The $(^{26}\text{Al}/^{27}\text{Al})_0$ values of Y20-1X1 and Y20-9-1 are $(4.8 \pm 0.5) \times 10^{-5}$ and $(4.9 \pm 0.3) \times 10^{-5}$, respectively, both of which are identical to the canonical $^{26}\text{Al}/^{27}\text{Al}$ ratio. Assuming the homogenous distribution of ^{26}Al with the canonical $^{26}\text{Al}/^{27}\text{Al}$ ratio at the CAI-forming region, the present CO CAIs formed within ~ 0.2 Myr after the birth of the Solar System. The $(^{10}\text{Be}/^9\text{Be})_0$ values of Y20-1X1 and Y20-9-1 are $(2.9 \pm 0.6) \times 10^{-3}$ and $(2.2 \pm 1.0) \times 10^{-3}$, respectively, which are significantly higher than the average $(^{10}\text{Be}/^9\text{Be})_0 = \sim 0.7 \times 10^{-3}$ of ^{26}Al -rich CAIs from CV chondrites. The apparent variation provides evidence for heterogeneous distribution of ^{10}Be at the birth of the Solar System and supports the solar cosmic ray irradiation origin of ^{10}Be . The present CO CAIs exhibit the group II-like REE pattern, suggesting the condensation of these CAIs or their precursors from a fractionated gas. Since high $(^{10}\text{Be}/^9\text{Be})_0$ values tend to be found in CAIs with the group II REE pattern, these types of CAIs or their precursors might have formed

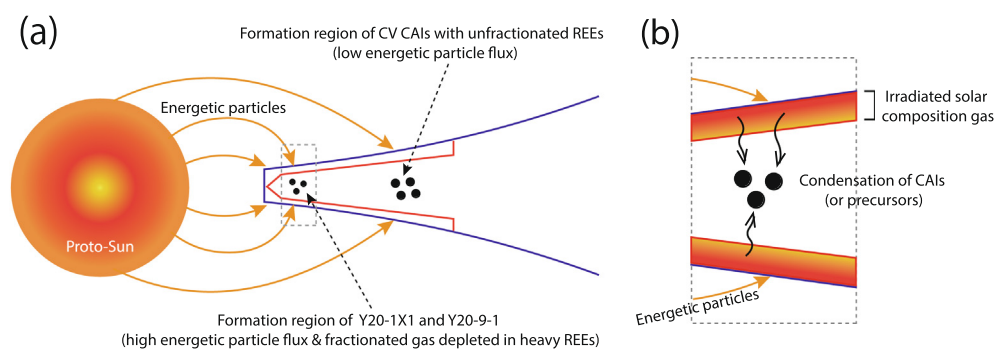


Fig. 10. (a) Schematic diagram for formation regions of the CAIs. If the present CO CAIs (Y20-1X1 and Y20-9-1) formed contemporaneously with the ^{26}Al -rich CV CAIs, the differences in their initial $^{10}\text{Be}/^9\text{Be}$ ratios can be understood as a result of their different formation locations. Since CAIs with a group II REE pattern tend to have high initial $^{10}\text{Be}/^9\text{Be}$ ratios (Sossi et al., 2017; this study), these CAI-forming gaseous reservoir would be located at the innermost parts of the solar protoplanetary disk. (b) Enlarged view of the region shown by the dotted rectangle in (a). CAIs or their precursors form by condensation from the irradiated gas. Because energetic particle fluxes decrease with distance from the Sun (e.g., Jacquet, 2019), ^{26}Al -rich CV CAIs with unfractionated REEs might have formed at outer regions than the present CO CAIs (Y20-1X1 and Y20-9-1). Alternatively, if all the ^{26}Al -rich CAIs formed at the same region, solar cosmic ray fluxes at the CAI-forming region would have fluctuated by a factor of six within a short duration (~ 0.2 Myr). See more discussions in Section 4.3.

at the innermost part of the solar protoplanetary disk. Alternatively, if the present CO CAIs formed in the same region as ^{26}Al -rich CV CAIs, solar energetic particle fluxes from the proto-Sun would have changed by a factor of six within a short duration (~ 0.2 Myr) at the CAI forming-region.

Declaration of Competing Interest

The authors declare that they have no known competing financial interests or personal relationships that could have appeared to influence the work reported in this paper.

ACKNOWLEDGMENT

We thank National Institute of Polar Research (NIPR, Japan) for providing the Yamato-81020 sample. We also thank Hiroshi Hidaka, Shogo Tachibana, Takashi Mikouchi, Makoto Kimura, and Mingming Zhang for their valuable comments, Naoto Takahata for assistance with NanoSIMS analyses, and Koji Ichimura for technical help with FE-EPMA analyses. We are grateful to Ritesh K. Mishra and two anonymous reviewers for constructive reviews that significantly improved the quality of the paper, and Audrey Bouvier for prompt editorial handling. This work was partly supported by JSPS KAKENHI grants No. 26400524 and 18K03720. WiscSIMS is partly supported by NSF Instrumentation and Facility Program (EAR-1658823). The upgrade of the RF plasma source is supported by the NASA Laboratory Analysis of Returned Samples and Planetary Major Equipment Programs (NNX16AG80G) and the NSF Instrumentation and Facility Program (EAR-1355590).

APPENDIX A. SUPPLEMENTARY DATA

Supplementary data to this article can be found online at <https://doi.org/10.1016/j.gca.2020.10.011>.

REFERENCES

- Amelin Y., Kaltenbach A., Iizuka T., Stirling C. H., Ireland T. R., Petaev M. and Jacobsen S. B. (2010) U-Pb chronology of the Solar System's oldest solids with variable $^{238}\text{U}/^{235}\text{U}$. *Earth Planet. Sci. Lett.* **300**, 343–350.
- Banerjee P., Qian Y. Z., Heger A. and Haxton W. C. (2016) Evidence from stable isotopes and ^{10}Be for solar system formation triggered by a low-mass supernova. *Nat. Commun.* **7**, 1–6.
- Bizzarro M., Baker J. A. and Haack H. (2004) Mg isotope evidence for contemporaneous formation of chondrules and refractory inclusions. *Nature* **431**, 275–278.
- Bouvier A. and Wadhwa M. (2010) The age of the solar system redefined by the oldest Pb-Pb age of a meteoritic inclusion. *Nat. Geosci.* **3**, 637–641.
- Boynnton W. V. (1975) Fractionation in the solar nebula: condensation of yttrium and the rare earth elements. *Geochim. Cosmochim. Acta* **39**, 569–584.
- Brand W. A., Coplen T. B., Vogl J., Rosner M. and Prohaska T. (2014) Assessment of international reference materials for isotope-ratio analysis (IUPAC technical report). *Pure Appl. Chem.* **86**, 425–467.
- Bricker G. E. and Caffee M. W. (2010) Solar wind implantation model for ^{10}Be in calcium-aluminum inclusions. *Astrophys. J.* **725**, 443–449.
- Chaussidon M. and Gounelle M. (2006) Irradiation processes in the early solar system. In *Meteorites and the early solar system II* (eds. D. S. Lauretta and H. Y. McSween). The University of Arizona Press, Arizona, pp. 323–339.
- Chaussidon M. and Liu M.-C. (2015) Timing of nebula processes that shaped the precursors of the terrestrial planets. In *The Early Earth: Accretion and Differentiation* (eds. J. Badro and M. Walter). American Geophysical Union, John Wiley & Sons, Inc., Washington, D.C. pp. 1–26.
- Chaussidon M., Robert F. and McKeegan K. D. (2006) Li and B isotopic variations in an Allende CAI: Evidence for the in situ decay of short-lived ^{10}Be and for the possible presence of the short-lived nuclide ^7Be in the early solar system. *Geochim. Cosmochim. Acta* **70**, 5433–5436.
- Connelly J. N., Bizzarro M., Krot A. N., Nordlund Å., Wielandt D. and Ivanova M. A. (2012) The absolute chronology and thermal processing of solids in the solar protoplanetary disk. *Science* **338**, 651–655.
- Davis A. M. and Grossman L. (1979) Condensation and fractionation of rare earths in the solar nebula. *Geochim. Cosmochim. Acta* **43**, 1611–1632.
- Davis A. M. and McKeegan K. D. (2014) Short-lived radionuclides and early solar system chronology. In *Treatise on Geochemistry* (eds. H. Holland and K. Turekian), 2nd Ed. Elsevier, Oxford, pp. 361–395.
- Desch S. J., Connolly H. C. J. and Srinivasan G. (2004) An interstellar origin for the Beryllium 10 in calcium-rich, aluminum-rich inclusions. *Astrophys. J.* **602**, 528–542.
- Dunham E. T., Liu M.-C., Hertwig A. T., Desch S. J. and Wadhwa M. (2019) CO₃ and CH/CB CAIs suggest ^{10}Be was distributed uniformly in the Solar nebula. In *82nd Annual Meeting of The Meteoritical Society*, Abstract #6346.
- Dunham E. T., Wadhwa M., Desch S. J. and Hervig R. L. (2020) Best practices for determination of initial $^{10}\text{Be}/^9\text{Be}$ in early Solar System materials by secondary ion mass spectrometry. *Geostand. Geoanalytical Res.*, 12329.
- Ferreira, T., Rasband, W., 2012. ImageJ User Guide. , 1–187. Available at: <https://imagej.nih.gov/ij/docs/user-guide.pdf>.
- Fowler W. A., Greenstein J. L. and Hoyle F. (1961) Deuteronomy. Synthesis of deuterons and the light nuclei during the early history of the solar system. *Am. J. Phys.* **29**, 393–403.
- Fowler W. A., Greenstein J. L. and Hoyle F. (1962) Nucleosynthesis during the early history of the solar system. *Geophys. J. R. Astron. Soc.* **6**, 148–220.
- Fujiya W., Hoppe P. and Ott U. (2016) Boron abundances and isotopic ratios of olivine grains on Itokawa returned by the Hayabusa spacecraft. *Meteorit. Planet. Sci.* **51**, 1721–1729.
- Fukuda K., Fujiya W., Hiyagon H., Makino Y., Sugiura N., Takahata N., Hirata T. and Sano Y. (2018) Beryllium-boron relative sensitivity factors for melilite glasses measured with a NanoSIMS ion microprobe. *Geochem. J.* **52**, 255–262.
- Fukuda K., Hiyagon H., Fujiya W., Takahata N., Kagoshima T. and Sano Y. (2019) Origin of the short-lived radionuclide ^{10}Be and its implications for the astronomical setting of CAI formation in the solar protoplanetary disk. *Astrophys. J.* **886**, 11 pp.
- Fukuda K., Beard B. L., Dunlap D. R., Spicuzza M. J., Fournelle J. H., Wadhwa M. and Kita N. T. (2020) Magnesium isotope analysis of olivine and pyroxene by SIMS: Evaluation of matrix effects. *Chem. Geol.* **540**, 119482.
- Fukuda K., Brownlee D. E., Joswiak D. J., Tenner T. J., Kimura M. and Kita N. T. (2021) Correlated isotopic and chemical evidence for condensation origins of olivine in comet 81P/Wild 2 and in AOAs from CV and CO chondrites. *Geochim. Cosmochim. Acta* **293**, 544–574. <https://doi.org/10.1016/j.gca.2020.09.036>.

- Galy A., Yoffe O., Janney P. E., Williams R. W., Cloquet C., Alard O., Halicz L., Wadhwa M., Hutcheon I. D., Ramon E. and Carignan J. (2003) Magnesium isotope heterogeneity of the isotopic standard SRM980 and new reference materials for magnesium-isotope-ratio measurements. *J. Anal. At. Spectrom.* **18**, 1352.
- Goswami J. N., Srinivasan G. and Ulyanov A. A. (1994) Ion microprobe studies of Efremovka CAIs: I. Magnesium isotope composition. *Geochim. Cosmochim. Acta* **58**, 431–447.
- Goswami J. N., Marhas K. K. and Sahijpal S. (2001) Did solar energetic particles produce the short-lived nuclides present in the early Solar System? *Astrophys. J.* **552**, 912.
- Gounelle M., Shu F. H., Shang H., Glassgold A. E., Rehm K. E. and Lee T. (2001) Extinct radioactivities and protosolar cosmic rays: Self-shielding and light elements. *Astrophys. J.* **548**, 1051–1070.
- Gounelle M., Shu F. H., Shang H., Glassgold A. E., Rehm K. E. and Lee T. (2006) The irradiation origin of beryllium radioisotopes and other short-lived radionuclides. *Astrophys. J.* **640**, 1163–1170.
- Gounelle M., Chaussidon M. and Rollion-Bard C. (2013) Variable and extreme irradiation conditions in the early solar system inferred from the initial abundance of ^{10}Be in isheyevo CAIs. *Astrophys. J. Lett.* **763**, 5 pp.
- Grossman J. N. and Brearley A. J. (2005) The onset of metamorphism in ordinary and carbonaceous chondrites. *Meteorit. Planet. Sci.* **40**, 87–122.
- Grossman J. N. and Rubin A. E. (2006) Dominion Range 03238: A possible missing link in the metamorphic sequence of CO3 chondrites. 37th Lunar Planet. Sci. Conf., #1383.
- Grossman L. (1975) Petrography and mineral chemistry of Ca-rich inclusions in the Allende meteorite. *Geochim. Cosmochim. Acta* **39**, 433–454.
- Han J., Keller L. P., Liu M. C., Needham A. W., Hertwig A. T., Messenger S. and Simon J. I. (2020) A coordinated microstructural and isotopic study of a Wark-Lovering rim on a Vigarano CAI. *Geochim. Cosmochim. Acta* **269**, 639–660.
- Hiyagon H., Yamakawa A., Ushikubo T., Lin Y. and Kimura M. (2011) Fractionation of rare earth elements in refractory inclusions from the Ningqiang meteorite: Origin of positive anomalies in Ce, Eu, and Yb. *Geochim. Cosmochim. Acta* **75**, 3358–3384.
- Holst J. C., Olsen M. B., Paton C., Nagashima K., Schiller M., Wielandt D., Larsen K. K., Connelly J. N., Jorgensen J. K., Krot A. N., Nordlund A. and Bizzarro M. (2013) ^{182}Hf - ^{182}W age dating of a ^{26}Al -poor inclusion and implications for the origin of short-lived radioisotopes in the early Solar System. *Proc. Natl. Acad. Sci.* **110**, 8819–8823.
- Ireland T. R., Fahey A. J. and Zinner E. K. (1988) Trace-element abundances in hibonites from the Murchison carbonaceous chondrite: Constraints on high-temperature processes in the solar nebula. *Geochim. Cosmochim. Acta* **52**, 2841–2854.
- Itano K. and Iizuka T. (2017) Unraveling the mechanism and impact of oxide production in LA-ICP-MS by comprehensive analysis of REE-Th-U phosphates. *J. Anal. At. Spectrom.* **32**, 2003–2010.
- Jacobsen B., Yin Q.-Z., Moynier F., Amelin Y., Krot A. N., Nagashima K., Hutcheon I. D. and Palme H. (2008) ^{26}Al - ^{26}Mg and ^{207}Pb - ^{206}Pb systematics of Allende CAIs: Canonical solar initial $^{26}\text{Al}/^{27}\text{Al}$ ratio reinstated. *Earth Planet. Sci. Lett.* **272**, 353–364.
- Jacquet E. (2019) Beryllium-10 production in gaseous protoplanetary disks and implications for the astrophysical setting of refractory inclusions. *Astron. Astrophys.* **624**, A131.
- Jaeger M., Wilmes S., Kölle V., Staudt G. and Mohr P. (1996) Precision measurement of the half-life of ^7Be . *Phys. Rev. C - Nucl. Phys.* **54**, 423–424.
- Jochum K. P., Weis U., Stoll B., Kuzmin D., Yang Q., Raczek I., Jacob D. E., Stracke A., Birbaum K., Frick D. A., Günther D. and Enzweiler J. (2011) Determination of reference values for NIST SRM 610–617 glasses following ISO guidelines. *Geoanalytical Res.* **35**, 397–429.
- Kasemann S. A., Jeffcoate A. B. and Elliott T. (2005) Lithium isotope composition of basalt glass reference material. *Anal. Chem.* **77**, 5251–5257.
- Kawasaki N., Itoh S., Sakamoto N. and Yurimoto H. (2017) Chronological study of oxygen isotope composition for the solar protoplanetary disk recorded in a fluffy Type A CAI from Vigarano. *Geochim. Cosmochim. Acta* **201**, 83–102.
- Kawasaki N., Simon S. B., Grossman L., Sakamoto N. and Yurimoto H. (2018) Crystal growth and disequilibrium distribution of oxygen isotopes in an igneous Ca-Al-rich inclusion from the Allende carbonaceous chondrite. *Geochim. Cosmochim. Acta* **221**, 318–341.
- Kawasaki N., Park C., Sakamoto N., Park S. Y., Kim H. N., Kuroda M. and Yurimoto H. (2019) Variations in initial $^{26}\text{Al}/^{27}\text{Al}$ ratios among fluffy Type A Ca–Al-rich inclusions from reduced CV chondrites. *Earth Planet. Sci. Lett.* **511**, 25–35.
- Kawasaki N., Wada S., Park C., Sakamoto N. and Yurimoto H. (2020) Variations in initial $^{26}\text{Al}/^{27}\text{Al}$ ratios among fine-grained Ca-Al-rich inclusions from reduced CV chondrites. *Geochim. Cosmochim. Acta* **279**, 1–15.
- Kimura M., Goresy A., El Palme H. and Zinner E. (1993) Ca-, Al-rich inclusions in the unique chondrite ALH85085: Petrology, chemistry and isotopic compositions. *Geochim. Cosmochim. Acta* **57**, 2329–2359.
- Kimura M., Grossman J. N. and Weisberg M. K. (2008) Fe-Ni metal in primitive chondrites: Indicators of classification and metamorphic conditions for ordinary and CO chondrites. *Meteorit. Planet. Sci.* **43**, 1161–1177.
- Kita N. T., Ushikubo T., Knight K. B., Mendybaev R. A., Davis A. M., Richter F. M. and Fournelle J. H. (2012) Internal ^{26}Al - ^{26}Mg isotope systematics of a Type B CAI: Remelting of refractory precursor solids. *Geochim. Cosmochim. Acta* **86**, 37–51.
- Kööp L., Davis A. M., Nakashima D., Park C., Krot A. N., Nagashima K., Tenner T. J., Heck P. R. and Kita N. T. (2016) A link between oxygen, calcium and titanium isotopes in ^{26}Al -poor hibonite-rich CAIs from Murchison and implications for the heterogeneity of dust reservoirs in the solar nebula. *Geochim. Cosmochim. Acta* **189**, 70–95.
- Kööp L., Nakashima D., Heck P. R., Kita N. T., Tenner T. J., Krot A. N., Nagashima K., Park C. and Davis A. M. (2018) A multielement isotopic study of refractory FUN and F CAIs: Mass-dependent and mass-independent isotope effects. *Geochim. Cosmochim. Acta* **221**, 296–317.
- Korschinek G., Bergmaier A., Faestermann T., Gerstmann U. C., Knie K., Rugel G., Wallner A., Dillmann I., Dollinger G., von Gostomski C. L., Kossert K., Maiti M., Poutivtsev M. and Remmert A. (2010) A new value for the half-life of ^{10}Be by heavy-ion elastic recoil detection and liquid scintillation counting. *Nucl. Instruments Methods Phys. Res. Sect. B Beam Interact. with Mater. Atoms* **268**, 187–191.
- Krot A. N., Petaev M. I., Russell S. S., Itoh S., Fagan T. J., Yurimoto H., Chizmadia L., Weisberg M. K., Komatsu M., Ulyanov A. A. and Keil K. (2004) Amoeboid olivine aggregates and related objects in carbonaceous chondrites: Records of nebular and asteroid processes. *Chem. Erde* **64**, 185–239.
- Krot A. N., Nagashima K., Bizzarro M., Huss G. R., Davis A. M., Meyer B. S. and Ulyanov A. A. (2008) Multiple generations of

- refractory inclusions in the metal-rich carbonaceous chondrites Acfer 182/214 and Isheyevo. *Astrophys. J.* **672**, 713–721.
- Krot A. N., Makide K., Nagashima K., Huss G. R., Oglione R. C., Ciesla F. J., Yang L., Hellebrand E. and Gaidos E. (2012) Heterogeneous distribution of ^{26}Al at the birth of the solar system: Evidence from refractory grains and inclusions. *Meteorit. Planet. Sci.* **47**, 1948–1979.
- Krot A. N., Nagashima K., Wasserburg G. J., Huss G. R., Papanastassiou D., Davis A. M., Hutcheon I. D. and Bizzarro M. (2014) Calcium-aluminum-rich inclusions with fractionation and unknown nuclear effects (FUN CAIs): I. Mineralogy, petrology, and oxygen isotopic compositions. *Geochim. Cosmochim. Acta* **145**, 206–247.
- Krot A. N., Nagashima K., Simon S. B., Ma C., Connolly H. C., Huss G. R., Davis A. M. and Bizzarro M. (2019) Mineralogy, petrography, and oxygen and aluminum-magnesium isotope systematics of grossite-bearing refractory inclusions. *Geochemistry* **79**, 125529.
- Larsen K. K., Trinquier A., Paton C., Schiller M., Wielandt D., Ivanova M. A., Connolly J. N., Nordlund Å., Krot A. N. and Bizzarro M. (2011) Evidence for magnesium isotope heterogeneity in the solar protoplanetary disk. *Astrophys. J. Lett.* **735**, 7 pp.
- Larsen K. K., Wielandt D., Schiller M., Krot A. N. and Bizzarro M. (2020) Episodic formation of refractory inclusions in the Solar System and their presolar heritage. *Earth Planet. Sci. Lett.* **535**, 116088.
- LaTourrette T. and Wasserburg G. J. (1998) Mg diffusion in anorthite: implications for the formation of early solar system planetesimals. *Earth Planet. Sci. Lett.* **158**, 91–108.
- Leya I., Halliday A. N. and Wieler R. (2003) The predictable collateral consequences of nucleosynthesis by spallation reactions in the early solar system. *Astrophys. J.* **594**, 605–616.
- Liu M.-C. and Chaussidon M. (2018) The cosmochemistry of boron isotopes. In *Advances in Isotope Geochemistry* (eds. H. Macschi and G. Foster). Springer, Berlin, pp. 273–289.
- Liu M.-C., McKeegan K. D., Goswami J. N., Marhas K. K., Sahijpal S., Ireland T. R. and Davis A. M. (2009) Isotopic records in CM hibonites: Implications for timescales of mixing of isotope reservoirs in the solar nebula. *Geochim. Cosmochim. Acta* **73**, 5051–5079.
- Liu M.-C., Nittler L. R., Alexander C. M. O. D. and Lee T. (2010) Lithium-beryllium-boron isotopic compositions in meteoritic hibonite: Implications for origin of ^{10}Be and early solar system irradiation. *Astrophys. J. Lett.* **719**, 99–103.
- Liu M.-C., Han J., Brearley A. J. and Hertwig A. T. (2019) Aluminum-26 chronology of dust coagulation and early solar system evolution. *Sci. Adv.* **5**, 1–8.
- Lodders K. (2003) Solar system abundances and condensation temperatures of the elements. *Astrophys. J.* **591**, 1220–1247.
- Ludwig K. R. (2012) User's Manual for Isoplot 3.75. Berkeley Geochronology Center, Special Publication. pp. 1–75.
- MacPherson G. J. (2014) Calcium-aluminum-rich inclusions in chondritic meteorites. In *Treatise on Geochemistry* (eds. H. Holland and K. Turekian), 2nd Edition. Elsevier, Oxford, pp. 139–179.
- Macpherson G. J. and Grossman L. (1984) “Fluffy” Type A Ca-, Al-rich inclusions in the Allende meteorite. *Geochim. Cosmochim. Acta* **48**, 29–46.
- MacPherson G. J., Huss G. R. and Davis A. M. (2003) Extinct ^{10}Be in Type A calcium-aluminum-rich inclusions from CV chondrites. *Geochim. Cosmochim. Acta* **67**, 3165–3179.
- MacPherson G. J., Bullock E. S., Janney P. E., Kita N. T., Ushikubo T., Davis A. M., Wadhwa M. and Krot A. N. (2010) Early solar nebula condensates with canonical, not supra-canonical, initial $^{26}\text{Al}/^{27}\text{Al}$ ratios. *Astrophys. J. Lett.* **711**, 117–121.
- MacPherson G. J., Kita N. T., Ushikubo T., Bullock E. S. and Davis A. M. (2012) Well-resolved variations in the formation ages for Ca-Al-rich inclusions in the early Solar System. *Earth Planet. Sci. Lett.* **331–332**, 43–54.
- Makide K., Nagashima K., Krot A. N., Huss G. R., Hutcheon I. D., Hellebrand E. and Petaev M. I. (2013) Heterogeneous distribution of ^{26}Al at the birth of the Solar System: Evidence from corundum-bearing refractory inclusions in carbonaceous chondrites. *Geochim. Cosmochim. Acta* **110**, 190–215.
- Marhas K. K., Goswami J. N. and Davis A. M. (2002) Short-lived nuclides in hibonite grains from Murchison: Evidence for solar system evolution. *Science* **298**, 2182–2185.
- Martin P. M. and Mason B. (1974) Major and trace elements in the Allende meteorite. *Nature* **249**, 333–334.
- McDonough W. F. and Sun S.- (1995) The composition of the Earth. *Chem. Geol.* **120**, 223–253.
- McKeegan K. D., Chaussidon M. and Robert F. (2000) Incorporation of short-lived ^{10}Be in a calcium-aluminum-rich inclusion from the Allende meteorite. *Science* **289**, 1334–1337.
- Mishra R. K. (2018) Petrography and mineralogy of calcium-, aluminum-rich inclusions in an unequilibrated carbonaceous chondrite Y 81020 (CO3.05). *Curr. Sci.* **114**, 1510–1519.
- Mishra R. K. and Chaussidon M. (2014) Timing and extent of Mg and Al isotopic homogenization in the early inner Solar System. *Earth Planet. Sci. Lett.* **390**, 318–326.
- Mishra R. K. and Marhas K. K. (2019) Meteoritic evidence of a late superflare as source of ^7Be in the early Solar System. *Nat. Astron.* **3**, 498–505.
- Nagahara H. and Ozawa K. (2000) Isotopic fractionation as a probe of heating processes in the solar nebula. *Chem. Geol.* **169**, 45–68.
- Nagasawa H., Schreiber H. D. and Morris R. V. (1980) Experimental mineral/liquid partition coefficients of the rare earth elements (REE), Sc and Sr for perovskite, spinel and melilite. *Earth Planet. Sci. Lett.* **46**, 431–437.
- Oglione R. C., Huss G. R. and Nagashima K. (2011) Ratio estimation in SIMS analysis. *Nucl. Instruments Methods Phys. Res. Sect. B Beam Interact. Mater. Atoms* **269**, 1910–1918.
- Olsen M. B., Krot A. N., Larsen K., Paton C., Wielandt D., Schiller M. and Bizzarro M. (2011) Whole-rock ^{26}Al - ^{26}Mg systematics of amoeboid olivine aggregates from the oxidized CV3 carbonaceous chondrite Allende. *Meteorit. Planet. Sci.* **46**, 1688–1702.
- Van Orman J. A., Cherniak D. J. and Kita N. T. (2014) Magnesium diffusion in plagioclase: Dependence on composition, and implications for thermal resetting of the ^{26}Al - ^{26}Mg early solar system chronometer. *Earth Planet. Sci. Lett.* **385**, 79–88.
- Palme H., Lodders K. and Jones A. (2014) Solar system abundances of the elements. In *Treatise on Geochemistry* (eds. H. D. Holland and K. K. Turekian), 2nd Ed. Elsevier, Oxford, pp. 15–36.
- Park C., Nagashima K., Krot A. N., Huss G. R., Davis A. M. and Bizzarro M. (2017) Calcium-aluminum-rich inclusions with fractionation and unidentified nuclear effects (FUN CAIs): II. Heterogeneities of magnesium isotopes and ^{26}Al in the early Solar System inferred from in situ high-precision magnesium-isotope measurements. *Geochim. Cosmochim. Acta* **201**, 6–24.
- Podosek F. A., Zinner E. K., Macpherson G. J., Lundberg L. L., Brannon J. C. and Fahey A. J. (1991) Correlated study of initial $^{87}\text{Sr}/^{86}\text{Sr}$ and Al-Mg isotopic systematics and petrologic properties in a suite of refractory inclusions from the Allende meteorite. *Geochim. Cosmochim. Acta* **55**, 1083–1110.

- Reeves H. (1994) On the origin of the light elements ($Z < 6$). *Rev. Mod. Phys.* **66**, 193–216.
- Richter F. M. (2004) Timescales determining the degree of kinetic isotope fractionation by evaporation and condensation. *Geochim. Cosmochim. Acta* **68**, 4971–4992.
- Richter F. M., Janney P. E., Mendybaev R. A., Davis A. M. and Wadhwa M. (2007) Elemental and isotopic fractionation of Type B CAI-like liquids by evaporation. *Geochim. Cosmochim. Acta* **71**, 5544–5564.
- Russell S. S., Huss G. R., Fahey A. J., Greenwood R. C., Hutchison R. and Wasserburg G. J. (1998) An isotopic and petrologic study of calcium-aluminum-rich inclusions from CO3 meteorites. *Geochim. Cosmochim. Acta* **62**, 689–714.
- Sahijpal S. and Goswami J. N. (1998) Refractory phases in primitive meteorites devoid of ^{26}Al and ^{41}Ca : Representative samples of first solar system solids? *Astrophys. J.* **509**, L137–L140.
- Seitz H. M., Brey G. P., Zipfel J., Ott U., Weyer S., Durali S. and Weinbruch S. (2007) Lithium isotope composition of ordinary and carbonaceous chondrites, and differentiated planetary bodies: Bulk solar system and solar reservoirs. *Earth Planet. Sci. Lett.* **260**, 582–596.
- Simon J. I., Young E. D., Russell S. S., Tonui E. K., Dyl K. A. and Manning C. E. (2005) A short timescale for changing oxygen fugacity in the solar nebula revealed by high-resolution ^{26}Al - ^{26}Mg dating of CAI rims. *Earth Planet. Sci. Lett.* **238**, 272–283.
- Simon S. B., Davis A. M. and Grossman L. (1999) Origin of compact type A refractory inclusions from CV3 carbonaceous chondrites. *Geochim. Cosmochim. Acta* **63**, 1233–1248.
- Simon S. B. and Grossman L. (2015) Refractory inclusions in the pristine carbonaceous chondrites DOM 08004 and DOM 08006. *Meteorit. Planet. Sci.* **50**, 1032–1049.
- Sossi P. A., Moynier F., Chaussidon M., Villeneuve J., Kato C. and Gounelle M. (2017) Early Solar System irradiation quantified by linked vanadium and beryllium isotope variations in meteorites. *Nat. Astron.* **1**, 1–17.
- Srinivasan G. and Chaussidon M. (2013) Constraints on ^{10}Be and ^{41}Ca distribution in the early solar system from ^{26}Al and ^{10}Be studies of Efremovka CAIs. *Earth Planet. Sci. Lett.* **374**, 11–23.
- Srinivasan G., Huss G. R. and Wasserburg G. J. (2000) A petrographic, chemical, and isotopic study of calcium-aluminum-rich inclusions and aluminum-rich chondrules from the Axtell (CV3) chondrite. *Meteorit. Planet. Sci.* **35**, 1333–1354.
- Sugiura N., Shuzou Y. and Ulyanov A. (2001) Beryllium-boron and aluminum-magnesium chronology of calcium-aluminum-rich inclusions in CV chondrites. *Meteorit. Planet. Sci.* **36**, 1397–1408.
- Tatischeff V., Duprat J. and De Séreville N. (2014) Light-element nucleosynthesis in a molecular cloud interacting with a supernova remnant and the origin of beryllium-10 in the protosolar nebula. *Astrophys. J.* **796**, 20 pp.
- Teng F. Z., Li W. Y., Ke S., Marty B., Dauphas N., Huang S., Wu F. Y. and Pourmand A. (2010) Magnesium isotopic composition of the Earth and chondrites. *Geochim. Cosmochim. Acta* **74**, 4150–4166.
- Thrane K., Nagashima K., Krot A. N. and Bizzarro M. (2008) Discovery of a new FUN CAI from a CV carbonaceous chondrite: Evidence for multistage thermal processing in the protoplanetary disk. *Astrophys. J.* **680**, L141–L144.
- Ushikubo T., Tenner T. J., Hiyagon H. and Kita N. T. (2017) A long duration of the ^{16}O -rich reservoir in the solar nebula, as recorded in fine-grained refractory inclusions from the least metamorphosed carbonaceous chondrites. *Geochim. Cosmochim. Acta* **201**, 103–122.
- Wasserburg G. J., Lee T. and Papanastassiou D. A. (1977) Correlated O and Mg isotopic anomalies in Allende inclusions: II. Magnesium. *Geophys. Res. Lett.* **4**, 299–302.
- Wielandt D., Nagashima K., Krot A. N., Huss G. R., Ivanova M. A. and Bizzarro M. (2012) Evidence for multiple sources of ^{10}Be in the early solar system. *Astrophys. J.* **748**, 7 pp.
- Yiou F., Baril M., de Citres J. D., Fontes P., Gradsztajn E. and Bernas R. (1968) Mass-spectrometric measurement of lithium, beryllium, and boron isotopes produced in ^{16}O by high-energy protons, and some astrophysical implications. *Phys. Rev.* **166**, 968–974.
- Zhai M., Nakamura E., Shaw Denis M. and Nakano T. (1996) Boron isotopes in meteorites and lunar rocks. *Geochim. Cosmochim. Acta* **60**, 4877–4881.
- Zhang M., Bonato E., King A. J., Russell S. S., Tang G. and Lin Y. (2020) Petrology and oxygen isotopic compositions of calcium-aluminum-rich inclusions in primitive CO3.0-3.1 chondrites. *Meteorit. Planet. Sci.* **55**, 911–935.

Associate editor: Audrey Bouvier